

# Gaia DR2 orbital properties of selected APOGEE giants with anomalously high levels of [N/Fe] in the bulge and halo of the Milky Way

José G. Fernández-Trincado,<sup>1,2\*</sup> Edmundo Moreno<sup>3</sup>, and Angeles Pérez-Villegas<sup>4</sup>

<sup>1</sup>*Instituto de Astronomía y Ciencias Planetarias, Universidad de Atacama, Copayapu 485, Copiapó, Chile*

<sup>2</sup>*Institut Utinam, CNRS UMR6213, Univ. Bourgogne Franche-Comté, OSU THETA, Observatoire de Besançon, BP 1615, 25010 Besançon Cedex, France*

<sup>3</sup>*Instituto de Astronomía, Universidad Nacional Autónoma de México, Apdo. Postal 70264, México D.F., 04510, México*

<sup>4</sup>*Universidade de São Paulo, IAG, Rua do Matão 1226, Cidade Universitária, São Paulo 05508-900, Brazil*

20 December 2024

## ABSTRACT

We have used a state-of-the-art orbital integration model in a more realistic gravitational potential, to explore the orbital properties of a sample of 76 selected N-rich stars across the Milky Way, using 6-dimensional information provided by Gaia and the APOGEE-2 survey. Orbits are integrated in the galaxy modelling algorithm *GravPot16*, which mimics the non-axisymmetric structure of the inner Milky Way. We present the more probable orbital elements using the newly measured proper motions from Gaia DR2 with existing line-of-sight velocities from APOGEE-2 survey and spectrophotometric distance estimations from the *StarHorse* code. We find that most of the N-rich stars, show typically maximum height to the Galactic plane below 1.5 kpc, and develop rather eccentric orbits, suggesting that these stars are confined in the inner regions of the Galaxy and are likely to be dynamically associated with a ‘classical bulge’. We show that  $\sim 10\%$  of the N-rich stars in the inner Galaxy share the orbital properties of the bar/bulge, having perigalactic and apogalactic distances, and maximum vertical excursion from the Galactic plane inside the bar region.

**Key words:** Galaxy: kinematics and dynamics (Galaxy): globular clusters: individual: NGC 6362

The advent of large spectroscopic surveys like APOGEE (Majewski et al. 2017) which is capable to see through the dusty part of the Milky Way, together with other complementary surveys such as Gaia-ESO survey (Gilmore et al. 2012; Randich et al. 2013, among other), clearly revealed that our own Galaxy hosts a significant population of peculiar abundance red giants residing preferentially in the inner regions of the Galaxy (e.g., Recio-Blanco et al. 2017; Schiavon et al. 2017; Fernández-Trincado et al. 2017c), with a few confirmed cases toward the disc and halo (Martell et al. 2016; Pereira et al. 2017; Fernández-Trincado et al. 2016a, 2017c; Reis et al. 2018; Koch et al. 2019).

The APOGEE high-resolution spectra ( $R \approx 22,500$ ) on the near-IR *H*-band ( $\lambda \sim 1.5\text{--}1.7 \mu\text{m}$ ) have shown that many of these stars are often typified by large nitrogen-overabundances ( $[\text{N}/\text{Fe}] \gtrsim +0.5$ , hereafter N-rich), accompa-

nied by decreased abundances of carbon ( $[\text{C}/\text{Fe}] \lesssim +0.15$ ), identified most obviously by their  $^{12}\text{C}^{16}\text{O}$ -band, enhanced  $^{12}\text{C}^{14}\text{N}$ -band features (see, e.g., Altmann et al. 2005; Martell & Grebel 2010; Martell et al. 2011; Lind et al. 2015; Martell et al. 2016; Fernández-Trincado et al. 2016a; Schiavon et al. 2017; Fernández-Trincado et al. 2017c, 2019), and other abundances of elements involved in proton-capture reactions, i.e., Mg and Al, often structured in coherent patterns. Furthermore, the vast majority of the N-rich stars investigated so far possess clear chemical abundance patterns on their light elements similar to the observed in *second-generation* globular cluster stars (group of stars as enhanced N and Al and depleted Mg, C and O abundances with respect to field at the same metallicity  $[\text{Fe}/\text{H}]$ ).

The implicit assumption, that a few APOGEE N-rich stars in the field are former members of large or smaller accreted satellites occurring perhaps up to a few Gyr ago has not actually been demonstrated, and the origin of such an abundance signature remains still debated and can be ascribed to different exotic events, including external mech-

\* E-mail: jfernandezt87@gmail.com or jfernandez@obs-besancon.fr

anisms, like a binary mass-transfer channel and/or "in-situ" formation.

The current best interpretation is that these chemically anomalous field giants are former globular cluster stars (Khoperskov et al. 2018; Savino & Posti 2019), and as such, play an important role in deciphering the early history of the Milky Way itself (Martell & Grebel 2010; Carollo et al. 2013; Kunder et al. 2014; Lind et al. 2015; Fernández-Trincado et al. 2015a,b, 2016a,b; Recio-Blanco et al. 2017; Koppelman et al. 2018; Helmi et al. 2018; Tang et al. 2019; Ibata et al. 2019), currently there is no real working explanation for the origin of the gamut of extreme light and heavy elements simultaneously intervening in the chemical composition of the newly identified anomalous field stars. One of the most dramatic results from the APOGEE survey was discovered by Fernández-Trincado et al. (2017c), they identified a more exotic clump (7 out of 11 stars) of giant stars in the metal-poor tail ( $[\text{Fe}/\text{H}] \lesssim -0.7$ ) of the thick disc metallicity distribution which exhibit significant Mg-underabundances with extreme enrichment in N and Al suggesting a possible link to extragalactic globular clusters (Pancino et al. 2017), which none of the well studied Galactic globular clusters in our own Galaxy can reproduce it. However, the dynamical history of such stars remains unexplored to date.

Beyond of the intrinsic value of identifying chemically anomalous field stars throughout the Milky Way and understand the related abundance phenomena, a satisfactory explanation for the unexplained chemical anomalies and its relation to the orbital parameters may also offer insight into the origin of such stars. The newly discovered N-rich stars in the Milky Way (e.g., Martell et al. 2016; Fernández-Trincado et al. 2016b, 2017c; Schiavon et al. 2017) have a number of essential parameters that remain unexplored. In an effort to remedy this deficiency, we conducted for the first time a dynamics characterisation of such stars to predict the orbital path across the Milky Way as well as reveal their birthplace in order to improve our understanding of their origins.

In this work we take advantage of the accurate proper motions of The European Space Agency's Gaia mission Second Data Release (DR2) archive (Lindegren et al. 2018; Arenou et al. 2018), complemented along with radial velocity from APOGEE-2 (Nidever et al. 2015) and spectrophotometric distance from *StarHorse* (Queiroz et al. 2018), which permit an unprecedented combination of precision to fully resolve the space velocity and position vectors in order to study for the first time the dynamical behavior of these stars across of the Milky Way in a more realistic (as far as possible) Galactic model, like *GravPot16*†.

This paper is outlined as follows. In §1, we start by describing the APOGEE and Gaia data set and a series of selection criteria. In §2, we present the details of the Galactic model, followed by a discussion of the constraints on the free parameters of the model and the choices for the fiducial parameter values. We then move on to discuss the kinematic and dynamic behavior of our N-rich stars in §3, including an exploration of how the results depend on the free parameters. We summarize our key findings and conclude in §4.

† <https://gravpot.utinam.cnrs.fr/>

## 1 DATA

The sample analysed in this work consist of N-rich stars located towards the bulge, disc and halo taken from Martell et al. (2016), Fernández-Trincado et al. (2016b), Schiavon et al. (2017) and Fernández-Trincado et al. (2017c). The apparent exclusivity of such stars is attributed to their unusual chemical compositions and relation to Galactic and extragalactic globular cluster stars. This phenomenon have been widely exploited in the APOGEE survey (Majewski et al. 2017) by the above authors and have been confirmed from optical follow-up observations (e.g., Pereira et al. 2017). *H*-band ( $\sim \lambda 1.5\text{--}1.7\mu\text{m}$ ) high-resolution ( $R\sim 22,500$ ) APOGEE spectra were obtained with the 300-fiber spectrograph installed on the 2.5m Telescope (Gunn et al. 2006) at the Apache Point Observatory as part of the Sloan Digital Sky Survey IV (Blanton et al. 2017). The reduction of the APOGEE spectra, as well as the determination of radial velocities, atmospheric parameters and stellar abundances were carried out by the ASPCAP pipeline (see Nidever et al. 2015; Zamora et al. 2015; Holtzman et al. 2015; García Pérez et al. 2016) using reduction scripts designed for the 14th data release of SDSS (DR14, Abolfathi et al. 2018; Jönsson et al. 2018; Holtzman et al. 2018). We refer the reader to Zasowski et al. (2013) and Zasowski et al. (2017) for full details regarding the targeting strategies for APOGEE and APOGEE-2.

Here, we use the unprecedented 6-dimensional information of these stars provided by *Gaia* and the APOGEE survey, to investigate for the first time the orbital characteristics for a subset of this population.

### 1.1 6-D datasets

By cross-matching APOGEE-2 data to the *Gaia* (Gaia Collaboration et al. 2018), we have found Gaia counterparts to most of the N-rich stars studied in Martell et al. (2016), Fernández-Trincado et al. (2016b), Schiavon et al. (2017) and Fernández-Trincado et al. (2017c), with 5-D phase-space information, and only 7 of these stars has *Gaia* radial velocity information, with uncertainties on the order of 0.3–11 km/s. Our study is primarily based on proper motions from the *Gaia* catalog (Lindegren et al. 2018; Arenou et al. 2018), and APOGEE line-of-sight velocity because the error is generally smaller compared to other catalogues. The typical APOGEE uncertainties in radial velocity for our sample are of order of  $\lesssim 2 \text{ km s}^{-1}$ .

In the following discussion (see §1.2), we use the revised spectrophotometric distances from the Bayesian *StarHorse* code (Queiroz et al. 2018) for those sources.

### 1.2 Distances

To obtain robust data, we employed precise spectrophotometric distances (with median distance uncertainties of  $\lesssim 2 \text{ kpc}$ ) estimated with the Bayesian *StarHorse* code (see, Queiroz et al. 2018, for more details) which combines atmospheric parameters ( $T_{\text{eff}}$ ,  $\log g$  and  $[\text{M}/\text{H}]$ ) from the processed ASPCAP pipeline (García Pérez et al. 2016), multiband photometric information (APASS, 2MASS, and All- WISE) and the *Gaia* astrometric information when available with a Bayesian approach along with their associated uncertainties,

accounting for the global *Gaia* parallax zero-point shift of  $-0.029$  mas (Lindegren et al. 2018; Arenou et al. 2018). As the parallax measurements can be uncertain (large  $> 22\%$  and extending all the way up to  $1400\%$  uncertainty in the most extreme case), especially for distant stars, i.e., those located towards the Galactic bulge and halo, we believe that the choice to use spectrophotometric distances is well motivated to a large and homogeneously analyzed sample of N-rich stars, therefore from hereafter we decide to adopt the **StarHorse** distance calculations for orbital integration we define later.

A total of 75 out of 77 objects have reliable spectrophotometric distances determined using the **StarHorse** code as listed in Table 1: (i) One N-rich star, TYC 5619-109-1, from Fernández-Trincado et al. (2016b); (ii) Four "halo" N-rich stars from Martell et al. (2016); (iii) eleven N-rich stars from Fernández-Trincado et al. (2017c), and (iv) 59 "bulge" N-rich stars from Schiavon et al. (2017).

We also find that 2 out of 77 N-rich stars have reliable parallaxes and proper motions in the *Gaia* catalog: 2M02491285+5534213 with  $\varpi/\sigma_\varpi > 20$  and  $\sigma_\varpi/\varpi < 4\%$ , star from (Fernández-Trincado et al. 2017c), and 2M17431507–2815570 with  $\varpi/\sigma_\varpi > 7$  and  $\sigma_\varpi/\varpi < 14\%$ , star from (Schiavon et al. 2017). These stars are also listed in Table 1, namely the **StarHorse** code produce an estimated distance for 2M02491285+5534213 in good agreement with the distance derived as inverse of the parallax, for this star. For the second star, 2M17431507–2815570, the **StarHorse** code does not provide distance estimation, which can be attributed to uncertainties in the extinction in that direction, since it lies in a region where the extinction is higher. However, the small uncertainty in parallax for this star make it ideal to estimate the total velocity vector accurately, which we have included in our analysis.

The final sample so selected amounts to a total of 76 objects, from which 75 have spectrophotometric distance estimated from the **StarHorse** code, while one star, 2M17431507–2815570, have reliable *Gaia* parallax.

Complementary spectro-photometric distance estimates. Leung & Bovy (2019) derived precise distances for the whole APOGEE DR14 spectra sample from a neural-network ("deep learning") by training on the APOGEE-DR14/*Gaia* overlap, and makes use of no Galaxy priors and are thus not biased by such a prior. The left panel of Figure 1 shows the comparison between **StarHorse** and the distances from Leung & Bovy (2019) as well as the distance uncertainty as a function of our two sets of inferred distances (panel b in the same figure). Here it is clear, that **StarHorse** distances have smaller uncertainties at larger ranges than the ones obtained by Leung & Bovy (2019). As a result of the more precise estimates and the extinction treatment, we decided to use the **StarHorse** distances derived by Queiroz et al. (2018) as the main distance set along this work.

## 2 THE MILKY WAY MODEL

In order to construct a comprehensive orbital study of selected N-rich stars across the Milky Way, we use a state-of-the-art orbital integration model in a more realistic (as far as possible) gravitational potential, that fits the structural

and dynamical parameters to the best we know of the recent knowledge of our Galaxy.

For the computations in this work, we have employed the rotating "boxy/peanut" bar of the novel Galactic potential model called **GravPot16** along other composite stellar components. The considered structural parameters of our bar model, e.g., mass, present-day orientation and pattern speeds, is within observational estimations that lie in the range of  $1.1 \times 10^{10} M_\odot$ ,  $20^\circ$  and  $30\text{--}50 \text{ km s}^{-1} \text{ kpc}$ , respectively. The density-profile of the adopted "boxy/peanut" bar is exactly the same as in Robin et al. (2012), while the mathematical formalism to derive the gravitational potential of this component, will be explained in a forthcoming paper (Fernandez-Trincado et al., in preparation).

**GravPot16** considers on a global scale a 3D steady-state gravitational potential for the Galaxy, modelled as the superposition of axisymmetric and non-axisymmetric components. The axisymmetric potential is made-up of the superposition of many composite stellar populations belonging to seven thin discs, for each  $i^{\text{th}}$  component of the thin disc, we implemented an Einasto density-profile law (e.g., Einasto 1979; Robin et al. 2003), superposed along with two thick disc components, each one following a simple hyperbolic secant squared decreasing vertically from the Galactic plane plus an exponential profile decreasing with Galactocentric radius as described in Robin et al. (2014), we also implemented the density-profile of the interstellar matter (ISM) component with a density mass as presented in Robin et al. (2003).

The model, also correctly accounts for the underlying stellar halo, modelled by a Hernquist profile as already described in Robin et al. (2014), and surrounded by a single spherical Dark Matter halo component Robin et al. (2003), no time dependence of the density profiles is assumed. Our dynamical model has been adopted in a score of papers (e.g., Fernández-Trincado et al. 2016b, 2017b,a; Recio-Blanco et al. 2017; Albareti et al. 2017; Helmi et al. 2018; Libralato et al. 2018; Schiappacasse-Ulloa et al. 2018; Tang et al. 2018, 2019; Minniti et al. 2018). For a more detailed discussion, we refer the readers to a forthcoming paper (Fernandez-Trincado et al. 2019, in preparation).

For reference, the Galactic convention adopted by this work is:  $X$ -axis is oriented toward  $l = 0^\circ$  and  $b = 0^\circ$ , and the  $Y$ -axis is oriented toward  $l = 90^\circ$  and  $b = 0^\circ$ , and the disc rotates toward  $l = 90^\circ$ ; the velocity are also oriented in these directions. In this convention, the Sun's orbital velocity vector are  $[U_\odot, V_\odot, W_\odot] = [11.1, 12.24, 7.25] \text{ km s}^{-1}$  (Brunthaler et al. 2011). The model has been rescaled to the Sun's galactocentric distance,  $8.3 \text{ kpc}$ , and the local rotation velocity of  $239 \text{ km s}^{-1}$ .

For the computation of Galactic orbits of our N-rich stars, we have employed a simple Monte Carlo approach and the Runge-Kutta algorithm of seventh-order elaborated by Fehlberg (1968). The uncertainties in the input data (e.g.,  $\alpha$ ,  $\delta$ , distance, proper motions and line-of-sight velocity errors), were randomly propagated as  $1\sigma$  variation in a Gaussian Monte Carlo re-sampling. For each N-rich star we computed thousand orbits, computed backward in time during 3 Gyr. The average value of the orbital elements was found for our 1000 realizations, with uncertainty ranges given by the 16th and 84th percentile values, as listed in Table 2. As an additional test, we also run our backwards

**Table 1.** N-rich stars with reliable parallax information from *Gaia*, from the which the distances were determined as inverse of the parallax ( $d = 1/\varpi$ ) with relative errors of  $<22\%$  at most, and compared to other distance estimation methods.

Gaia-Id	APOGEE-ID	RV $\pm \Delta$ km s <sup>-1</sup>	$\mu_{\alpha} \cos \delta \pm \Delta$ mas yr <sup>-1</sup>	$\mu_{\delta} \pm \Delta$ mas yr <sup>-1</sup>	$d_{\odot} \pm \Delta$ kpc	Source	Comments
4342924973847237760	2M16011638–1201525	84.07 $\pm$ 0.88	-11.707 $\pm$ 0.098	-18.001 $\pm$ 0.058	2.8 $\pm$ 0.29	StarHorse	FT+16
454457984314449664	2M02491285+5534213	-222.31 $\pm$ 0.08	41.086 $\pm$ 0.067	0.096 $\pm$ 0.072	1.27 $\pm$ 0.05	StarHorse	FT+17
454457984314449664	2M02491285+5534213				1.32 $\pm$ 0.06	<i>Gaia</i>	FT+17
3572729757329728256	2M11462612–1419069	98.01 $\pm$ 0.27	-1.479 $\pm$ 0.081	-2.219 $\pm$ 0.049	3.59 $\pm$ 0.42	StarHorse	FT+17
3921278138790077312	2M12155306+1431114	100.55 $\pm$ 0.57	-1.007 $\pm$ 0.118	-1.421 $\pm$ 0.099	13.59 $\pm$ 1.22	StarHorse	FT+17
4343242938866170880	2M16062302–1126161	-105.93 $\pm$ 0.35	-6.367 $\pm$ 0.094	-9.04 $\pm$ 0.045	3.62 $\pm$ 0.39	StarHorse	FT+17
4108129758998519296	2M17180311–2750124	-113.63 $\pm$ 0.13	-3.125 $\pm$ 0.073	-5.46 $\pm$ 0.047	3.37 $\pm$ 0.43	StarHorse	FT+17
4060291416819133056	2M17350460–2856477	-106.56 $\pm$ 0.51	-0.411 $\pm$ 0.303	-9.896 $\pm$ 0.237	4.42 $\pm$ 0.5	StarHorse	FT+17
4060839287187830016	2M17454705–2639109	-75.5 $\pm$ 0.01	-0.533 $\pm$ 0.258	-5.531 $\pm$ 0.225	4.88 $\pm$ 0.96	StarHorse	FT+17
4068656265170572288	2M17492967–2328298	26.12 $\pm$ 0.03	0.891 $\pm$ 0.143	-8.78 $\pm$ 0.099	6.51 $\pm$ 1.06	StarHorse	FT+17
4056482502383480832	2M17534571–2949362	-140.4 $\pm$ 0.04	-4.898 $\pm$ 0.113	-4.764 $\pm$ 0.114	3.5 $\pm$ 0.57	StarHorse	FT+17
1351014402846463360	2M17535944+4708092	-266.21 $\pm$ 0.35	-1.201 $\pm$ 0.035	-2.071 $\pm$ 0.036	15.06 $\pm$ 1.66	StarHorse	FT+17
4069131112360013440	2M17585001–2338546	40.19 $\pm$ 0.02	-5.255 $\pm$ 2.031	-8.061 $\pm$ 1.631	2.83 $\pm$ 0.38	StarHorse	FT+17
3686800240419830912	2M13251355–0044438	-99.61 $\pm$ 0.28	-3.47 $\pm$ 0.067	-3.594 $\pm$ 0.044	14.98 $\pm$ 2.09	StarHorse	M+16
1291972861817776256	2M15113526+3551140	-246.5 $\pm$ 0.38	-2.14 $\pm$ 0.028	-1.833 $\pm$ 0.029	19.09 $\pm$ 2.19	StarHorse	M+16
4420577192280259840	2M15204588+0055032	-55.88 $\pm$ 0.06	-2.798 $\pm$ 0.057	-2.687 $\pm$ 0.053	18.52 $\pm$ 2.24	StarHorse	M+16
1366340710584081152	2M17252263+4903137	-249.73 $\pm$ 0.54	-1.56 $\pm$ 0.035	-0.693 $\pm$ 0.038	23.65 $\pm$ 2.47	StarHorse	M+16
676040916395844864	2M18550318–3043368	140.72 $\pm$ 0.14	-2.731 $\pm$ 0.075	-1.177 $\pm$ 0.064	9.74 $\pm$ 0.88	StarHorse	S+17
4127381662144718080	2M16493657–2028146	65.48 $\pm$ 0.99	-5.38 $\pm$ 0.049	-3.02 $\pm$ 0.029	7.45 $\pm$ 0.85	StarHorse	S+17
4127066926948887936	2M16514646–2120701	54.22 $\pm$ 0.54	-5.692 $\pm$ 0.052	-6.061 $\pm$ 0.031	4.97 $\pm$ 0.5	StarHorse	S+17
4126039261540147968	2M17024730–2210387	-21.67 $\pm$ 0.01	-5.279 $\pm$ 0.07	-2.674 $\pm$ 0.039	6.1 $\pm$ 0.6	StarHorse	S+17
4112528950908544000	2M17134700–2441353	-61.83 $\pm$ 0.02	-8.127 $\pm$ 0.091	-6.582 $\pm$ 0.063	10.64 $\pm$ 0.79	StarHorse	S+17
4109464119438841152	2M17161691–2458586	92.93 $\pm$ 0.01	-1.789 $\pm$ 0.086	-2.423 $\pm$ 0.057	8.41 $\pm$ 1.75	StarHorse	S+17
4111023643593381888	2M17173203–2439094	5.34 $\pm$ 0.01	-4.081 $\pm$ 0.142	-9.016 $\pm$ 0.093	7.54 $\pm$ 0.66	StarHorse	S+17
4107975252534509056	2M17193271–2735214	183.18 $\pm$ 0.01	-1.763 $\pm$ 0.097	-4.944 $\pm$ 0.063	9.61 $\pm$ 0.6	StarHorse	S+17
4059404282735445376	2M17205201–2903061	-8.22 $\pm$ 0.36	-2.221 $\pm$ 0.138	-6.01 $\pm$ 0.096	6.41 $\pm$ 0.83	StarHorse	S+17
4107966825115918336	2M17211817–2735530	-10.2 $\pm$ 0.01	-3.03 $\pm$ 0.171	-7.702 $\pm$ 0.124	7.48 $\pm$ 0.81	StarHorse	S+17
4111253785114563456	2M17263951–2406247	-52.35 $\pm$ 0.01	-3.642 $\pm$ 0.165	-5.5 $\pm$ 0.117	9.29 $\pm$ 1.36	StarHorse	S+17
4061493045593102720	2M17271907–2718040	63.38 $\pm$ 0.01	-9.02 $\pm$ 0.212	-7.034 $\pm$ 0.156	4.04 $\pm$ 0.59	StarHorse	S+17
4111402734583638144	2M17303980–2330234	-15.34 $\pm$ 0.01	-5.518 $\pm$ 0.117	-1.103 $\pm$ 0.086	8.14 $\pm$ 0.76	StarHorse	S+17
4061568813142719872	2M17305251–2651528	42.85 $\pm$ 0.24	1.065 $\pm$ 0.218	-7.97 $\pm$ 0.161	7.19 $\pm$ 0.89	StarHorse	S+17
4062064830323106048	2M17333623–2548156	81.3 $\pm$ 0.02	-4.034 $\pm$ 0.232	-4.13 $\pm$ 0.175	8.65 $\pm$ 1.38	StarHorse	S+17
4058532026206077504	2M17334208–2958347	90.12 $\pm$ 0.61	-2.476 $\pm$ 0.346	-4.266 $\pm$ 0.28	5.41 $\pm$ 0.69	StarHorse	S+17
4060282964322868736	2M17341660–2905083	-24.35 $\pm$ 0.07	-4.872 $\pm$ 0.315	-4.618 $\pm$ 0.252	4.44 $\pm$ 0.56	StarHorse	S+17
4060278673741274112	2M17343610–2909472	40.38 $\pm$ 0.53	-5.73 $\pm$ 0.567	-3.886 $\pm$ 0.461	6.51 $\pm$ 0.87	StarHorse	S+17
4121502431729496960	2M17343654–1956596	-7.47 $\pm$ 0.35	-6.494 $\pm$ 0.097	-1.413 $\pm$ 0.072	7.4 $\pm$ 1.21	StarHorse	S+17
4062000508887193472	2M17343807–2557555	-84.67 $\pm$ 0.01	-4.197 $\pm$ 0.221	-6.219 $\pm$ 0.173	5.74 $\pm$ 0.6	StarHorse	S+17
4058581130871346560	2M17350446–2932289	42.75 $\pm$ 0.98	0.746 $\pm$ 0.312	-0.566 $\pm$ 0.247	5.79 $\pm$ 0.92	StarHorse	S+17
4060091271345069312	2M17352288–2913255	46.58 $\pm$ 1.44	-3.445 $\pm$ 0.337	-5.194 $\pm$ 0.243	6.27 $\pm$ 1.13	StarHorse	S+17
4060508536008544128	2M17353215–2759106	18.07 $\pm$ 0.24	-1.052 $\pm$ 0.368	-3.509 $\pm$ 0.308	8.88 $\pm$ 1.42	StarHorse	S+17
4116366544202001664	2M17354267–2406233	-21.67 $\pm$ 0.01	-2.114 $\pm$ 0.342	1.162 $\pm$ 0.205	7.71 $\pm$ 0.83	StarHorse	S+17
4060484449833449088	2M17382269–2748001	-123.56 $\pm$ 0.3	-4.069 $\pm$ 0.204	-7.201 $\pm$ 0.148	9.38 $\pm$ 0.6	StarHorse	S+17
4057003159810599680	2M17390422–2943520	53.09 $\pm$ 0.54	0.246 $\pm$ 0.534	-9.785 $\pm$ 0.4	5.18 $\pm$ 0.89	StarHorse	S+17
4060898415964496128	2M17404143–2714570	-74.8 $\pm$ 0.01	-6.255 $\pm$ 0.371	-8.076 $\pm$ 0.281	8.03 $\pm$ 0.9	StarHorse	S+17
4060889448072712832	2M17415271–2715374	-46.99 $\pm$ 0.01	-5.652 $\pm$ 0.814	-5.647 $\pm$ 0.725	9.3 $\pm$ 1.17	StarHorse	S+17
406109969665413888	2M17434675–2616068	175.65 $\pm$ 0.01	-9.289 $\pm$ 0.194	-5.559 $\pm$ 0.149	7.75 $\pm$ 0.94	StarHorse	S+17
4061046785697602560	2M17442343–2627304	-210.17 $\pm$ 0.01	-4.172 $\pm$ 0.213	-6.128 $\pm$ 0.156	8.32 $\pm$ 0.96	StarHorse	S+17
4068740652650462464	2M17453131–2342147	97.36 $\pm$ 0.11	0.122 $\pm$ 0.132	-4.41 $\pm$ 0.094	10.48 $\pm$ 1.25	StarHorse	S+17
40671537418168181120	2M17464449–2531533	-37.09 $\pm$ 0.08	-5.407 $\pm$ 0.273	-7.466 $\pm$ 0.23	12.89 $\pm$ 1.61	StarHorse	S+17
4068061291921021568	2M17480576–2445000	-76.93 $\pm$ 0.02	-0.44 $\pm$ 0.404	-3.511 $\pm$ 0.316	7.64 $\pm$ 0.93	StarHorse	S+17
4068869497301335808	2M17482995–2305299	-216.43 $\pm$ 0.01	-1.07 $\pm$ 0.108	-6.557 $\pm$ 0.079	9.16 $\pm$ 1.37	StarHorse	S+17
4068671108581470976	2M17494963–2318560	-42.61 $\pm$ 0.01	0.044 $\pm$ 0.142	-4.218 $\pm$ 0.112	6.3 $\pm$ 1.12	StarHorse	S+17
4068711068966503552	2M17504980–2255083	46.99 $\pm$ 0.01	-6.615 $\pm$ 0.119	0.318 $\pm$ 0.096	6.54 $\pm$ 1.12	StarHorse	S+17
4057335384106810240	2M17514916–2859341	42.05 $\pm$ 0.37	-4.58 $\pm$ 0.245	-4.645 $\pm$ 0.201	8.44 $\pm$ 1.42	StarHorse	S+17
4056157596706349696	2M17523300–3027521	152.58 $\pm$ 0.51	-4.386 $\pm$ 0.227	-12.31 $\pm$ 0.185	8.93 $\pm$ 1.06	StarHorse	S+17
4057387198618922496	2M17524451–2830199	-50.0 $\pm$ 0.17	-0.493 $\pm$ 0.392	-5.68 $\pm$ 0.349	8.05 $\pm$ 0.87	StarHorse	S+17
4057382834998497024	2M17530277–2835196	-25.31 $\pm$ 1.78	-7.468 $\pm$ 0.28	-10.208 $\pm$ 0.223	7.55 $\pm$ 0.79	StarHorse	S+17
4063390394726120064	2M17534394–2826411	-124.71 $\pm$ 0.12	-3.605 $\pm$ 0.45	-12.784 $\pm$ 0.362	8.39 $\pm$ 0.68	StarHorse	S+17
407060607723206720	2M17554454–2123058	94.49 $\pm$ 0.04	-6.147 $\pm$ 0.213	-8.865 $\pm$ 0.196	5.16 $\pm$ 0.81	StarHorse	S+17
4050162475212092160	2M18014817–3026237	-21.21 $\pm$ 0.94	-4.336 $\pm$ 0.087	-6.729 $\pm$ 0.073	7.28 $\pm$ 0.92	StarHorse	S+17
4050281055043258496	2M18022530–2928338	157.52 $\pm$ 0.01	-3.273 $\pm$ 0.229	-3.117 $\pm$ 0.178	5.5 $\pm$ 0.76	StarHorse	S+17
4050198243675106688	2M18032356–3001588	-13.49 $\pm$ 2.18	2.509 $\pm$ 0.091	-6.507 $\pm$ 0.074	6.48 $\pm$ 0.96	StarHorse	S+17
4050360387280733568	2M18033335–2929122	-55.67 $\pm$ 0.18	-1.128 $\pm$ 0.12	-4.461 $\pm$ 0.095	6.74 $\pm$ 0.98	StarHorse	S+17
4050386195823196928	2M18035944–2908195	172.44 $\pm$ 0.01	-7.924 $\pm$ 0.094	-4.367 $\pm$ 0.077	6.41 $\pm$ 0.68	StarHorse	S+17
4050189383167644288	2M18045107–3002378	211.42 $\pm$ 0.97	-2.133 $\pm$ 0.307	-5.44 $\pm$ 0.253	7.34 $\pm$ 1.03	StarHorse	S+17
4049111410791537152	2M18054875–3122407	3.5 $\pm$ 0.44	-0.538 $\pm$ 0.093	-5.081 $\pm$ 0.077	9.35 $\pm$ 0.68	StarHorse	S+17
4043082174445050368	2M18061336–3147053	-57.46 $\pm$ 0.42	-1.048 $\pm$ 0.067	-7.261 $\pm$ 0.055	7.23 $\pm$ 1.02	StarHorse	S+17
4145860428221492480	2M18090957–1559276	-9.58 $\pm$ 0.01	-1.241 $\pm$ 0.387	-3.377 $\pm$ 0.372	9.56 $\pm$ 2.57	StarHorse	S+17
4063015014565121664	2M18102953–2707208	-51.67 $\pm$ 0.01	-7.512 $\pm$ 0.11	-7.332 $\pm$ 0.092	7.51 $\pm$ 1.92	StarHorse	S+17
4147311719145163648	2M18120031–1350169	-34.32 $\pm$ 0.01	-1.49 $\pm$ 0.271	-7.726 $\pm$ 0.234	5.75 $\pm$ 0.87	StarHorse	S+17
4050466352715069056	2M18121957–2926310	45.2 $\pm$ 0.13	-1.83 $\pm$ 0.066	-4.317 $\pm$ 0.056	8.59 $\pm$ 1.19	StarHorse	S+17
4052474099675496960	2M18124455–2719146	-156.9 $\pm$ 0.01	-4.469 $\pm$ 0.121	-4.008 $\pm$ 0.103	7.47 $\pm$ 0.75	StarHorse	S+17
4094363495457944576	2M18165340–2017051	69.49 $\pm$ 0.06	-4.575 $\pm$ 0.316	-5.94 $\pm$ 0.278	8.41 $\pm$ 2.41	StarHorse	S+17
4048286162963631872	2M18334592–2903253	-151.82 $\pm$ 0.02	-3.308 $\pm$ 0.046	-5.788 $\pm$ 0.04	6.2 $\pm$ 0.61	StarHorse	S+17
4047570930629411072	2M18372953–2911046	36.52 $\pm$ 0.02	-1.545 $\pm$ 0.06	-2.157 $\pm$ 0.051	7.38 $\pm$ 0.85	StarHorse	S+17
6737355836773067392	2M18442352–3029411	-63.86 $\pm$ 0.34	0.363 $\pm$ 0.082	-6.258 $\pm$ 0.069	4.89 $\pm$ 0.56	StarHorse	S+17
406052793062410624	2M17431507–2815570	-72.58 $\pm$ 0.31	-2.518 $\pm$ 0.196	-0.573 $\pm$ 0.162	1.09 $\pm$ 0.14	<i>Gaia</i>	S+17

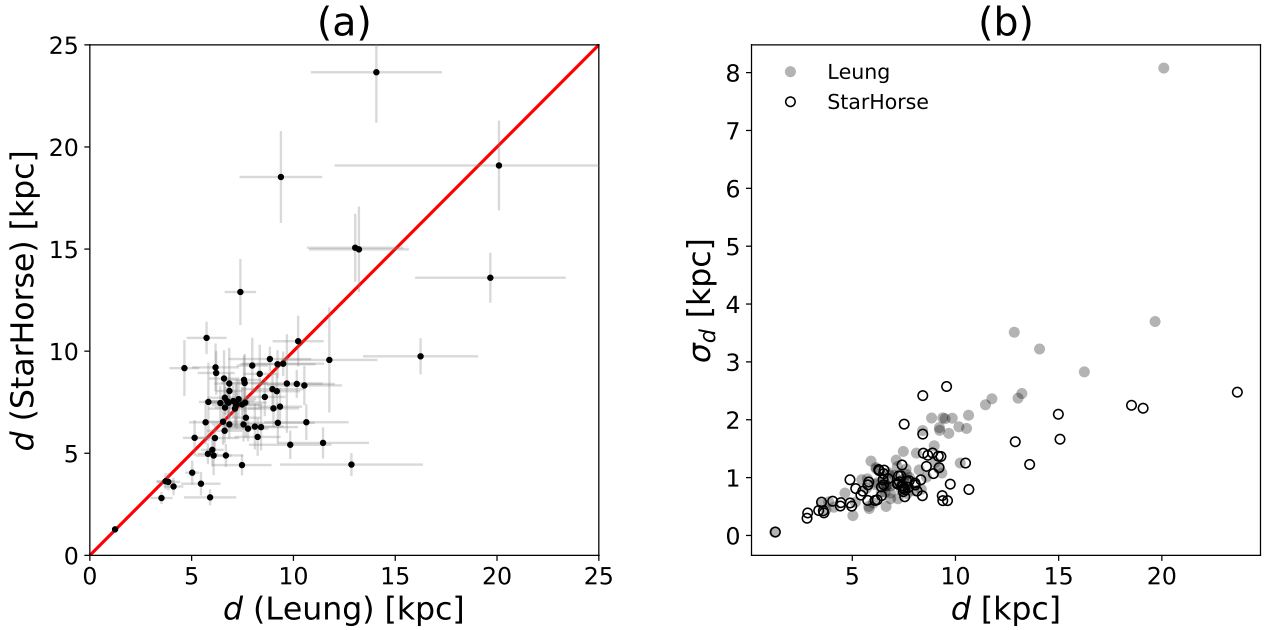


**Figure 1.** Comparison between our inferred distances from **StarHorse** and the distances from **Leung & Bovy (2019)**. In panel (a) the red solid line marks the 1:1 relation. The panel (b) shows the uncertainty as a function of distances.

N-rich stars identified in the inner Galaxy (e.g., **Schiavon et al. 2017**) which were supposed to belong to the Galactic bulge, therefore one would expect that most of our stars follow the typical orbital configurations of the bulge region, with a few exceptions as will be discussed below.

Figure 2 shows the shape of the orbit displayed by the mean orbital eccentricity<sup>1</sup> ( $e$ ) against the amplitude of the vertical oscillation ( $|Z_{max}|$ ) for each N-rich star. The dashed horizontal line in the same figure represents the edge  $|Z_{max}|$  of the thick disk,  $Z = 3$  kpc (**Carollo et al. 2010**). Our N-rich star sample has median  $e$  of 0.89 and median  $|Z_{max}|$  of 1.3 kpc, which is dynamically consistent with both bulge and inner-halo population. There are a few stars with  $|Z_{max}| \gtrsim 3$  kpc and larger eccentricities ( $\gtrsim 0.5$ ), this suggest that most of these stars belong to the inner-halo, especially we confirm that all of N-rich stars analyzed in (**Martell et al. 2016**) are mostly consistet with the Galactic (inner) halo and are characterized by eccentric orbits ( $e \gtrsim 0.8$ ) that can extend, on average,  $\lesssim 18.6 \pm 3.2$  kpc out the Galactic plane.

On the other hand, we find two N-rich stars from **Schiavon et al. (2017)** in orbits with  $|Z_{max}| \lesssim 3$  kpc and lower eccentricities ( $\lesssim 0.5$ ): the star 2M17464449–2531533 has an  $e \sim 0.5$  with  $|Z_{max}| \sim 1.5$  kpc, given these orbital properties, we expect it is a thick-disk contaminate, but more important, the orbit of this star have energies allowing this star to cross the bar’s corotation radius (CR  $\sim 6.5$  kpc), in this region two class of orbits appears around the Lagrange points  $L_4$  and  $L_5$  on the minor axis of the bar that can be stable, depending the bar pattern speed: a pure

banana-like orbit (for a slow rotating bar of  $35 \text{ km s}^{-1} \text{ kpc}^{-1}$ ), with orbits that circulate  $L_4$  and  $L_5$ , and orbits trapped around CR for a while (for a faster rotating bar of  $50 \text{ km s}^{-1} \text{ kpc}^{-1}$ ), the results are illustrated in Figure 7; the second star, 2M17431507–2815570, has an  $e < 0.5$  with  $|Z_{max}| < 0.5$  kpc, with an in-plane orbit confined inside the inner bar region ( $r_{gal} \lesssim 0.5$  kpc), the orbit is trapped by a higher-order resonance, depending on the bar patterns speed, such orbits have been also identified in bulge globular clusters (see, e.g., **Pérez-Villegas et al. 2018**).

For comparison, we plot our N-rich stars in the space of a characteristic orbital energy,  $E_{char} = (E_{max} + E_{min})/2$  as defined in **Moreno et al. (2015)**, versus the orbital Jacobi constant ( $E_J$ ) in the reference frame of the bar, along with the expected Galactic trend of globular clusters (see Figure 3) adopting the inputs parameters of the late compilation of clusters properties given by **Vasiliev (2018)**. This figure clearly shows the trends between the less bound (inner) halo N-rich stars (less negative orbital energies) against the more bound N-rich stars (more negative orbital energies), which have very similar orbital properties as observed in Galactic globular clusters. More general, these results provides observational support for the idea that the inner/outer stellar halo may have been assembled by kicking out captured possibly globular cluster stars with its own chemical enrichment history (e.g., **Nissen & Schuster 2010; Carollo et al. 2013; Kunder et al. 2014; Fernández-Trincado et al. 2015a,b, 2016b,a; Koppelman et al. 2018; Khoperskov et al. 2018**). In other words, these stars have presumably migrated from stellar clusters into the inner-halo.

For each generated set of orbits, we calculate the perigalactic distance  $r_{per}$ , and the apogalactic distance  $r_{apo}$ ,

<sup>1</sup> the eccentricity  $e$ , is defined as  $(r_{apo} - r_{per}) / (r_{apo} + r_{per})$

**Table 2.** Orbital elements obtained using a simple Monte Carlo approach for the N-rich stars studied in this work. The average value of the orbital elements (pericentric and apocentric radii, the eccentricity, the maximum distance the orbit reaches above/below the Galactic plane as well as the maximum and minimum of the z-component of the angular momentum in the inertial frame,  $L_z$ ) was found for the half million realizations, with uncertainty ranges given by the 16th (*subscript*) and 84th (*superscript*) percentile values.

$\Omega_{bar}$ km s <sup>-1</sup> kpc <sup>-1</sup>	APOGEE-ID	$\langle r_{min} \rangle$ kpc	$\langle r_{max} \rangle$ kpc	$\langle e \rangle$	$\langle  Z_{max}  \rangle$ kpc	$\langle L_{z,min} \rangle$ km s <sup>-1</sup> kpc <sup>-1</sup>	$\langle L_{z,max} \rangle$ km s <sup>-1</sup> kpc <sup>-1</sup>
35	2M17535944+4708092	2.03 <sub>1.38</sub> <sup>3.08</sup>	16.97 <sub>15.39</sub> <sup>19.31</sup>	0.78 <sub>0.72</sub> <sup>0.83</sup>	9.55 <sub>9.17</sub> <sup>9.99</sup>	-85.0 <sub>-125.0</sub> <sup>-50.0</sup>	-102.0 <sub>-134.0</sub> <sup>-74.0</sup>
40	2M17535944+4708092	2.20 <sub>1.41</sub> <sup>2.98</sup>	17.31 <sub>15.67</sub> <sup>19.67</sup>	0.77 <sub>0.73</sub> <sup>0.83</sup>	9.64 <sub>9.32</sub> <sup>9.97</sup>	-93.0 <sub>-121.0</sub> <sup>-57.0</sup>	-107.0 <sub>-134.0</sub> <sup>-80.0</sup>
45	2M17535944+4708092	2.21 <sub>1.60</sub> <sup>3.03</sup>	17.62 <sub>15.71</sub> <sup>20.46</sup>	0.77 <sub>0.74</sub> <sup>0.81</sup>	9.77 <sub>9.47</sub> <sup>10.07</sup>	-92.0 <sub>-124.0</sub> <sup>-64.84</sup>	-101.0 <sub>-142.0</sub> <sup>-78.0</sup>
50	2M17535944+4708092	2.17 <sub>1.63</sub> <sup>3.14</sup>	18.53 <sub>15.51</sub> <sup>19.39</sup>	0.78 <sub>0.72</sub> <sup>0.80</sup>	9.96 <sub>9.59</sub> <sup>10.30</sup>	-91.0 <sub>-128.0</sub> <sup>-65.0</sup>	-110.0 <sub>-136.0</sub> <sup>-75.0</sup>
35	2M17585001-2338546	1.07 <sub>0.71</sub> <sup>2.36</sup>	5.99 <sub>5.37</sub> <sup>6.19</sup>	0.68 <sub>0.44</sub> <sup>0.77</sup>	0.46 <sub>0.06</sub> <sup>0.81</sup>	-37.0 <sub>-75.0</sub> <sup>-26.0</sup>	-93.0 <sub>-101.0</sub> <sup>-69.0</sup>
40	2M17585001-2338546	1.72 <sub>1.23</sub> <sup>2.30</sup>	5.84 <sub>5.44</sub> <sup>6.23</sup>	0.54 <sub>0.44</sub> <sup>0.64</sup>	0.45 <sub>0.06</sub> <sup>0.85</sup>	-57.0 <sub>-72.0</sub> <sup>-42.0</sup>	-87.0 <sub>-103.16</sub> <sup>-75.0</sup>
45	2M17585001-2338546	1.56 <sub>0.93</sub> <sup>2.13</sup>	5.74 <sub>5.44</sub> <sup>6.20</sup>	0.57 <sub>0.47</sub> <sup>0.71</sup>	0.51 <sub>0.06</sub> <sup>1.00</sup>	-51.0 <sub>-66.0</sub> <sup>-32.0</sup>	-83.0 <sub>-102.0</sub> <sup>-69.0</sup>
50	2M17585001-2338546	1.40 <sub>0.95</sub> <sup>1.80</sup>	5.77 <sub>5.41</sub> <sup>5.58</sup>	0.63 <sub>0.55</sub> <sup>0.71</sup>	0.46 <sub>0.07</sub> <sup>0.71</sup>	-46.0 <sub>-55.0</sub> <sup>-33.0</sup>	-84.0 <sub>-120.0</sub> <sup>-68.0</sup>
35	2M17350460-2856477	0.54 <sub>0.21</sub> <sup>0.84</sup>	4.49 <sub>3.91</sub> <sup>5.22</sup>	0.78 <sub>0.72</sub> <sup>0.89</sup>	2.18 <sub>1.71</sub> <sup>2.61</sup>	-15.0 <sub>-26.0</sub> <sup>-5.0</sup>	-46.0 <sub>-63.0</sub> <sup>-36.0</sup>
40	2M17350460-2856477	0.46 <sub>0.06</sub> <sup>0.77</sup>	4.73 <sub>3.96</sub> <sup>5.08</sup>	0.82 <sub>0.72</sub> <sup>0.96</sup>	2.09 <sub>1.70</sub> <sup>2.57</sup>	-12.0 <sub>-23.0</sub> <sup>0.0</sup>	-60.0 <sub>-73.0</sub> <sup>-35.0</sup>
45	2M17350460-2856477	0.49 <sub>0.20</sub> <sup>0.73</sup>	4.47 <sub>4.00</sub> <sup>5.27</sup>	0.80 <sub>0.74</sub> <sup>0.90</sup>	1.97 <sub>1.66</sub> <sup>2.38</sup>	-14.0 <sub>-23.0</sub> <sup>-4.0</sup>	-50.0 <sub>-63.16</sub> <sup>-39.0</sup>
50	2M17350460-2856477	0.45 <sub>0.18</sub> <sup>0.87</sup>	4.70 <sub>3.85</sub> <sup>5.21</sup>	0.81 <sub>0.70</sub> <sup>0.91</sup>	1.97 <sub>1.65</sub> <sup>2.32</sup>	-13.0 <sub>-28.0</sub> <sup>-4.0</sup>	-50.0 <sub>-60.0</sub> <sup>-34.0</sup>
35	2M12155306+1431114	2.90 <sub>2.51</sub> <sup>3.29</sup>	16.08 <sub>15.04</sub> <sup>17.29</sup>	0.69 <sub>0.64</sub> <sup>0.74</sup>	14.46 <sub>13.42</sub> <sup>15.59</sup>	-94.0 <sub>-103.0</sub> <sup>-85.0</sup>	-100.0 <sub>-110.0</sub> <sup>-90.0</sup>
40	2M12155306+1431114	2.96 <sub>2.58</sub> <sup>3.36</sup>	16.19 <sub>15.17</sub> <sup>17.60</sup>	0.69 <sub>0.74</sub> <sup>0.74</sup>	14.52 <sub>13.29</sub> <sup>15.85</sup>	-98.0 <sub>-107.0</sub> <sup>-88.0</sup>	-100.0 <sub>-109.0</sub> <sup>-92.0</sup>
45	2M12155306+1431114	2.98 <sub>2.56</sub> <sup>3.38</sup>	16.34 <sub>15.24</sub> <sup>17.82</sup>	0.69 <sub>0.64</sub> <sup>0.74</sup>	14.66 <sub>13.32</sub> <sup>16.09</sup>	-98.0 <sub>-107.0</sub> <sup>-87.0</sup>	-102.0 <sub>-110.0</sub> <sup>-93.0</sup>
50	2M12155306+1431114	2.92 <sub>2.51</sub> <sup>3.34</sup>	15.91 <sub>15.08</sub> <sup>17.11</sup>	0.69 <sub>0.64</sub> <sup>0.74</sup>	14.40 <sub>13.38</sub> <sup>15.51</sup>	-95.0 <sub>-105.0</sub> <sup>-85.0</sup>	-99.0 <sub>-109.0</sub> <sup>-89.0</sup>
35	2M16062302-1126161	0.45 <sub>0.34</sub> <sup>0.57</sup>	5.49 <sub>5.21</sub> <sup>5.84</sup>	0.84 <sub>0.80</sub> <sup>0.88</sup>	3.90 <sub>3.77</sub> <sup>4.09</sup>	-10.0 <sub>-12.0</sub> <sup>-6.0</sup>	-37.0 <sub>-52.0</sub> <sup>-26.0</sup>
40	2M16062302-1126161	0.34 <sub>0.07</sub> <sup>1.04</sup>	5.52 <sub>5.26</sub> <sup>6.24</sup>	0.88 <sub>0.71</sub> <sup>0.97</sup>	3.85 <sub>3.27</sub> <sup>4.24</sup>	-6.0 <sub>-30.0</sub> <sup>2.0</sup>	-39.0 <sub>-60.0</sub> <sup>-27.84</sup>
45	2M16062302-1126161	0.39 <sub>0.19</sub> <sup>0.85</sup>	5.53 <sub>5.31</sub> <sup>5.93</sup>	0.86 <sub>0.74</sub> <sup>0.93</sup>	3.47 <sub>3.14</sub> <sup>3.79</sup>	-11.0 <sub>-27.0</sub> <sup>-3.0</sup>	-37.0 <sub>-52.16</sub> <sup>-30.0</sup>
50	2M16062302-1126161	0.51 <sub>0.25</sub> <sup>0.85</sup>	5.50 <sub>5.22</sub> <sup>5.19</sup>	0.83 <sub>0.78</sub> <sup>0.90</sup>	3.40 <sub>3.10</sub> <sup>3.86</sup>	-15.0 <sub>-26.0</sub> <sup>-6.0</sup>	-37.0 <sub>-77.0</sub> <sup>-26.0</sup>
35	2M17454705-2639109	0.78 <sub>0.37</sub> <sup>1.67</sup>	3.62 <sub>2.75</sub> <sup>4.70</sup>	0.64 <sub>0.48</sub> <sup>0.75</sup>	0.49 <sub>0.38</sub> <sup>0.60</sup>	-23.0 <sub>-51.0</sub> <sup>-10.0</sup>	-61.0 <sub>-77.16</sub> <sup>-48.0</sup>
40	2M17454705-2639109	0.77 <sub>0.43</sub> <sup>1.27</sup>	3.64 <sub>2.75</sub> <sup>4.64</sup>	0.64 <sub>0.55</sub> <sup>0.73</sup>	0.50 <sub>0.38</sub> <sup>0.61</sup>	-23.0 <sub>-39.0</sub> <sup>-12.0</sup>	-59.0 <sub>-89.0</sub> <sup>-48.0</sup>
45	2M17454705-2639109	0.72 <sub>0.32</sub> <sup>1.44</sup>	3.79 <sub>2.73</sub> <sup>4.70</sup>	0.67 <sub>0.53</sub> <sup>0.75</sup>	0.53 <sub>0.39</sub> <sup>0.66</sup>	-21.0 <sub>-43.0</sub> <sup>-8.0</sup>	-65.5 <sub>-86.0</sub> <sup>-45.0</sup>
50	2M17454705-2639109	0.61 <sub>0.40</sub> <sup>1.55</sup>	3.71 <sub>2.83</sub> <sup>4.73</sup>	0.69 <sub>0.51</sub> <sup>0.74</sup>	0.56 <sub>0.39</sub> <sup>0.75</sup>	-17.0 <sub>-45.0</sub> <sup>-10.0</sup>	-71.0 <sub>-84.0</sub> <sup>-48.0</sup>
35	2M17492967-2328298	0.17 <sub>0.03</sub> <sup>0.35</sup>	1.97 <sub>1.39</sub> <sup>3.24</sup>	0.83 <sub>0.77</sub> <sup>0.96</sup>	1.19 <sub>0.95</sub> <sup>1.53</sup>	-3.0 <sub>-9.0</sub> <sup>3.0</sup>	-26.0 <sub>-44.16</sub> <sup>-16.0</sup>
40	2M17492967-2328298	0.09 <sub>0.01</sub> <sup>0.31</sup>	2.14 <sub>1.29</sub> <sup>3.17</sup>	0.90 <sub>0.78</sub> <sup>0.98</sup>	1.23 <sub>0.96</sub> <sup>1.62</sup>	-1.0 <sub>-8.0</sub> <sup>5.0</sup>	-25.0 <sub>-40.0</sub> <sup>-13.0</sup>
45	2M17492967-2328298	0.14 <sub>0.01</sub> <sup>0.32</sup>	2.01 <sub>1.31</sub> <sup>3.11</sup>	0.87 <sub>0.78</sub> <sup>0.97</sup>	1.25 <sub>1.00</sub> <sup>1.56</sup>	-2.0 <sub>-7.0</sub> <sup>4.0</sup>	-24.5 <sub>-36.0</sub> <sup>-12.0</sup>
50	2M17492967-2328298	0.13 <sub>0.02</sub> <sup>0.23</sup>	2.24 <sub>1.36</sub> <sup>3.16</sup>	0.87 <sub>0.80</sub> <sup>0.97</sup>	1.24 <sub>0.98</sub> <sup>1.52</sup>	-2.0 <sub>-4.0</sub> <sup>4.0</sup>	-27.0 <sub>-34.0</sub> <sup>-11.0</sup>
35	2M17534571-2949362	1.30 <sub>0.89</sub> <sup>2.12</sup>	5.79 <sub>5.61</sub> <sup>6.58</sup>	0.62 <sub>0.51</sub> <sup>0.70</sup>	0.70 <sub>0.58</sub> <sup>0.82</sup>	-44.0 <sub>-70.0</sub> <sup>-31.84</sup>	-84.0 <sub>-97.0</sub> <sup>-78.0</sup>
40	2M17534571-2949362	1.52 <sub>0.89</sub> <sup>2.11</sup>	5.84 <sub>5.10</sub> <sup>6.85</sup>	0.58 <sub>0.52</sub> <sup>0.69</sup>	0.78 <sub>0.55</sub> <sup>0.99</sup>	-51.0 <sub>-70.0</sub> <sup>-30.0</sup>	-81.0 <sub>-100.0</sub> <sup>-68.0</sup>
45	2M17534571-2949362	1.55 <sub>0.99</sub> <sup>2.02</sup>	5.89 <sub>5.38</sub> <sup>8.14</sup>	0.60 <sub>0.57</sub> <sup>0.68</sup>	1.03 <sub>0.58</sub> <sup>1.67</sup>	-51.0 <sub>-67.0</sub> <sup>-33.0</sup>	-81.0 <sub>-117.0</sub> <sup>-71.0</sup>
50	2M17534571-2949362	1.44 <sub>1.08</sub> <sup>1.67</sup>	7.32 <sub>5.22</sub> <sup>7.69</sup>	0.64 <sub>0.62</sub> <sup>0.69</sup>	0.88 <sub>0.56</sub> <sup>1.56</sup>	-48.0 <sub>-56.0</sub> <sup>-35.0</sup>	-99.0 <sub>-107.0</sub> <sup>-69.0</sup>

Note: Table 2 is published in its entirety in a public repository at

[https://github.com/Fernandez-Trincado/N-rich-Stars/tree/master/Fernandez-Trincado%2B2019\\_Orbits/](https://github.com/Fernandez-Trincado/N-rich-Stars/tree/master/Fernandez-Trincado%2B2019_Orbits/)

the distribution of the average of these quantities are displayed in Figure 4 in both an axisymmetric model and a model including the Galactic bar potential. We found that most of the N-rich stars are characterized by close perigalactic passages, on average,  $\lesssim 1$  kpc out of the Galactic center with energies allowing them to have orbits inward and around the bar's CR radius, while the apogalactic distance are larger than CR ( $\gtrsim 6.5$  kpc) for a few cases, especially for those N-rich stars in halo-like orbits (sub-sample from Martell et al. 2016; Fernández-Trincado et al. 2016b, 2017c), implying that these stars should on average be older. We also found two stars (2M17464449-2531533 and 2M17431507-2815570) in (Schiavon et al. 2017) sample with larger apogalactic distance  $\gtrsim 9$  kpc and lower vertical excursion from the Galactic plane ( $\lesssim 2$ ) kpc, the most likely is that these two stars are halo (inner) interlopers that happens to be at same distance and location as where bulge N-rich stars reside, suggesting that contamination from disk

stars is relevant when attempting to trace this anomalous population, this is also supported by the dynamical behavior of N-rich stars from Fernández-Trincado et al. (2017c) in disk-like orbits also with lower vertical excursions from the Galactic plane as seen in Figure 2. However, there is not any obvious dependence among the metallicity and orbital properties, they were likely formed during the very early stages of the evolution of the Milky Way.

Following a similar interpretation as in Pérez-Villegas et al. (2018), we calculate the z-component of the angular momentum ( $L_z$ ) in the inertial frame, as this quantity is not conserved in a model with nonaxisymmetric structures, we are interested only in the sign, in order to know whether the orbital motion of the N-rich stars has a prograde or a retrograde sense with respect to the Galactic rotation. For this reason in Figure 5 we plot the maximum and minimum of the z-component of the angular momentum. In general, most (about 46%) of the N-rich stars lie in prograde orbits,

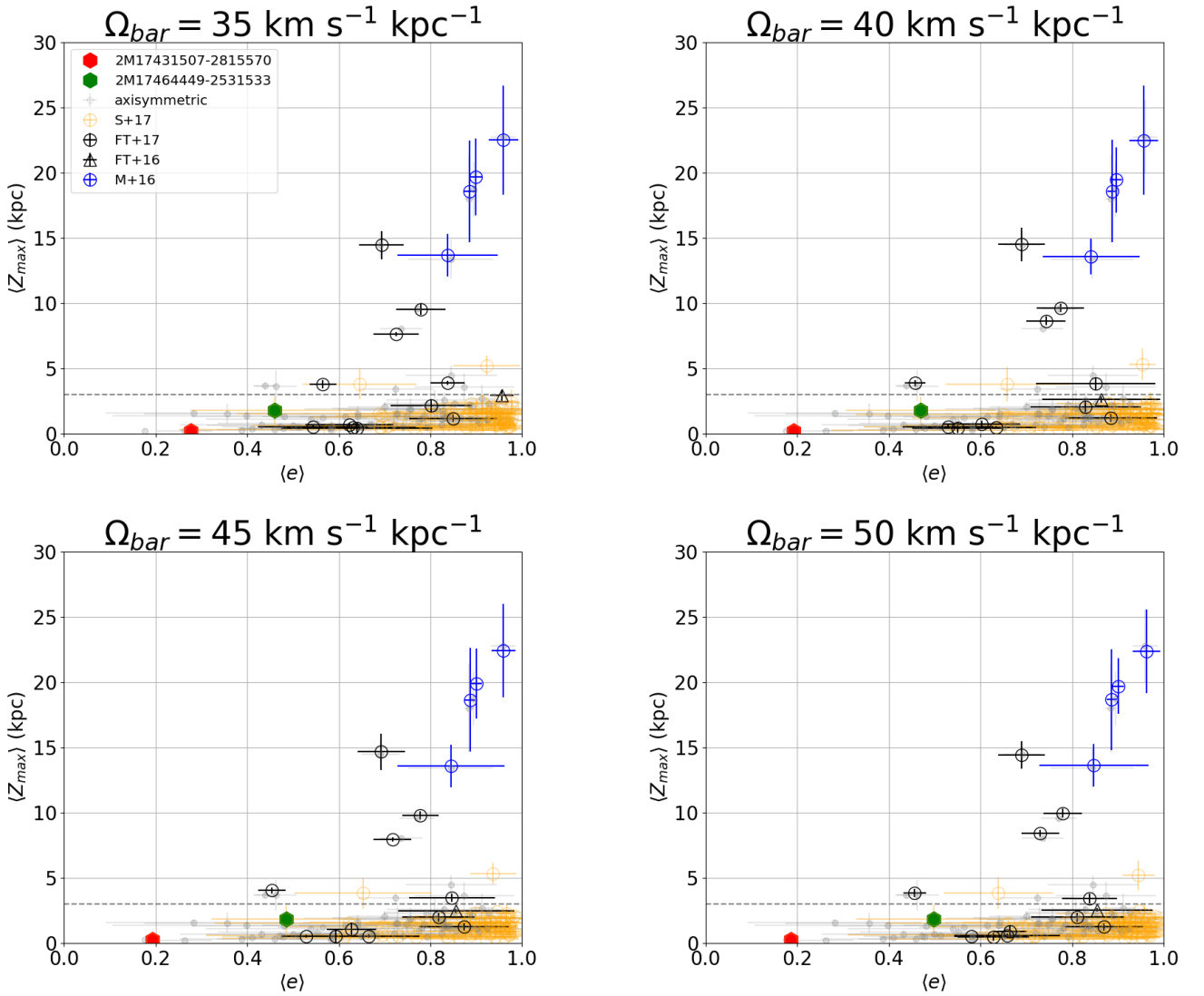


**Figure 2.** Distribution of N-rich stars in orbital-parameter space (shown is the average of the eccentricity,  $e$ , versus the maximum vertical excursion from the Galactic plane,  $|Z_{max}|$ ), for four different bar patterns speed as indicated in the title of each panel against the orbital solutions in the axisymmetric model (grey dot symbols). The orange unfilled circles, blue unfilled circles, black unfilled triangle and black unfilled circles highlight the N-rich stars from [Schiavon et al. \(2017\)](#), [Martell et al. \(2016\)](#), [Fernández-Trincado et al. \(2016b\)](#) and [Fernández-Trincado et al. \(2017c\)](#), respectively. The red and green filled hexagons mark the two N-rich stars highlighted in the text, 2M17431507–2815570 and 2M17464449–2531533, respectively. The dashed horizontal line represents the edge  $|Z_{max}| \sim 3$  kpc of the thick disk (e.g., [Carollo et al. 2010](#)). The error bar are computed with uncertainty ranges given by the 16<sup>th</sup> (subscript) and 84<sup>th</sup> (superscript) percentile values.

while a significant fraction (about 50% depending on the bar angular velocity) of the N-rich stars identified in [Schiavon et al. \(2017\)](#) toward the bulge region have prograde and retrograde orbits at the same time (green symbols in Figure 5), it is not surprising as such dynamical behavior have been observed in bulge globular clusters (see, e.g., [Pérez-Villegas et al. 2018](#)), such orbital properties could be related to an early chaotic phase of the evolution of the central regions of the Milky Way (see, e.g., [Pichardo et al. 2004](#); [Pérez-](#)

[Villegas et al. 2018](#)), this provides observational support for the idea that most of such unusual stars in the inner Galaxy may have been assembled by kicking out globular cluster stars ([Minniti et al. 2018](#); [Kunder et al. 2018](#)). Actually, most of these stars are bound objects to the Galaxy only for heliocentric distances smaller than  $\lesssim 25$  kpc. In the case of the axisymmetric model we found about 54% of the N-rich stars have orbits in a retrograde sense respect to the direction of the Galactic rotation, this orbital property could

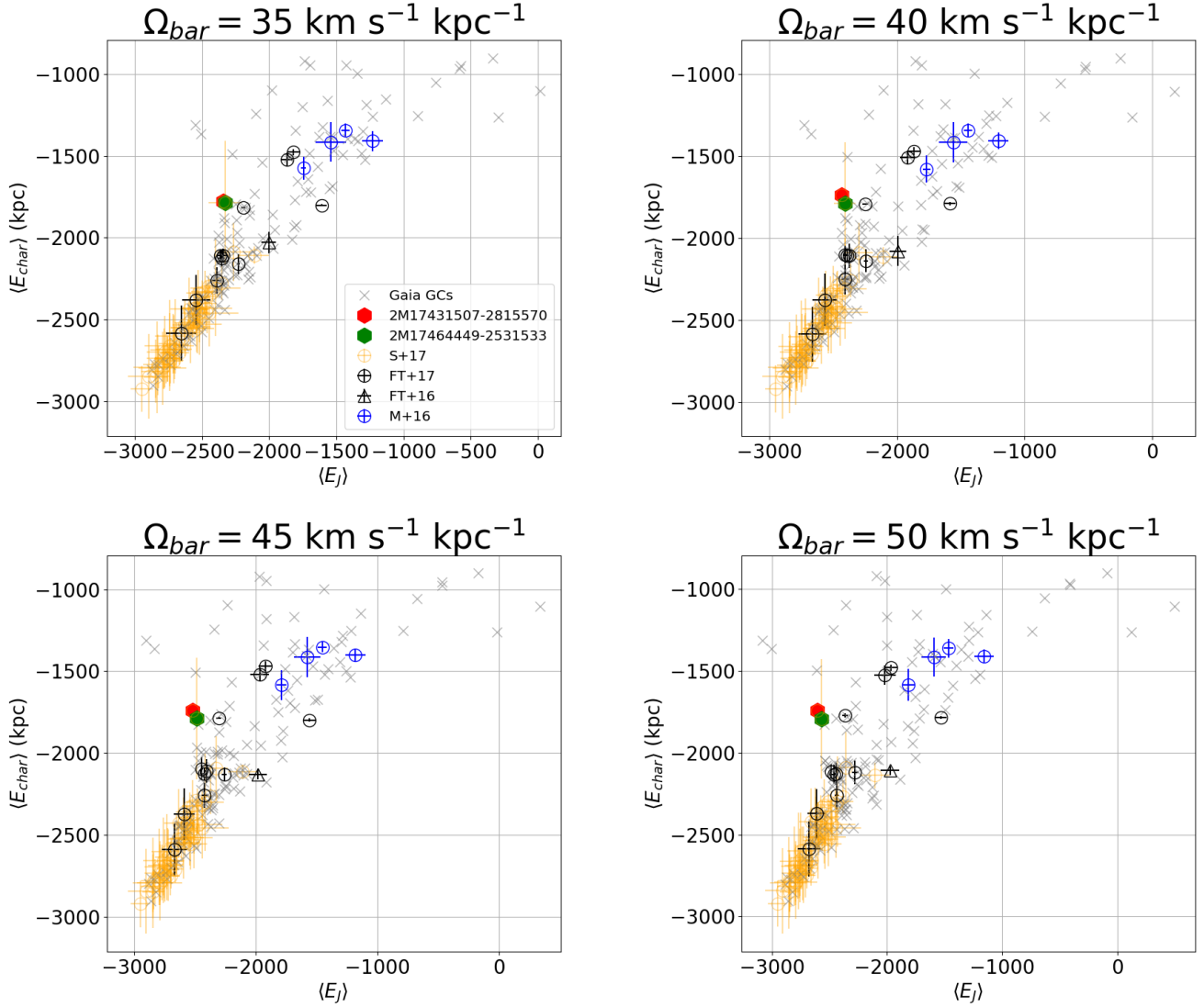


**Figure 3.** Similar to Figure 2, here for the Galactic potential model including only the boxy bar in its non-axisymmetric components. In this case, the diagram plots the average of a 'characteristic' orbital energy (see text),  $E_{char}$ , versus the orbital Jacobi constant ( $E_J$ ), in units of  $10^5 \text{ km}^2 \text{ s}^{-1}$ , computed in the reference frame of the bar. The symbols are similar as Figure 2, except the grey 'x' symbols, which represents the orbital properties of Galactic globular clusters adopting the recomputed information from [Vasiliev \(2018\)](#).

be indicative of an early chaotic phase of the evolution of the Milky Way bulge, meaning that such stars were likely formed in a very early stage of the Galaxy, probably before bar formation, and a few of them were trapped by the bar structure later on.

It is also worth mentioning that in addition to the bulge N-rich stars there is another object in prograde-retrograde orbit, depending on the bar patterns speed. The prograde-retrograde star is TYC 5619-109-1 an extremely N-rich star studied in [Fernández-Trincado et al. \(2016b\)](#), which exhibit a significant retrograde signature, with respect to the Galactic rotation, which is trapped by a higher-order resonance

inward CR (see Figure 7 and 8) in a potential with a faster bar ( $\gtrsim 40 \text{ km s}^{-1} \text{ kpc}^{-1}$ ), this retrograde sense is also seen in case of the potential as shown in Figure 9 and 10. When the slow ( $\sim 35 \text{ km s}^{-1} \text{ kpc}^{-1}$ ) is introduced to the model, there is an interesting dynamical effect produced, the star exhibit a dual motion in prograde-retrograde sense and going inside and outside of CR with low vertical excursion from the plane ( $|Z_{max}| \lesssim 2 \text{ kpc}$ ), we found this particular giant star is classified as a 'high-probability' (inner) stellar halo star, with a characteristic chaotic behavior.

Additionally, a few N-rich stars classified as "halo" stars in [Martell et al. \(2016\)](#), we found that four

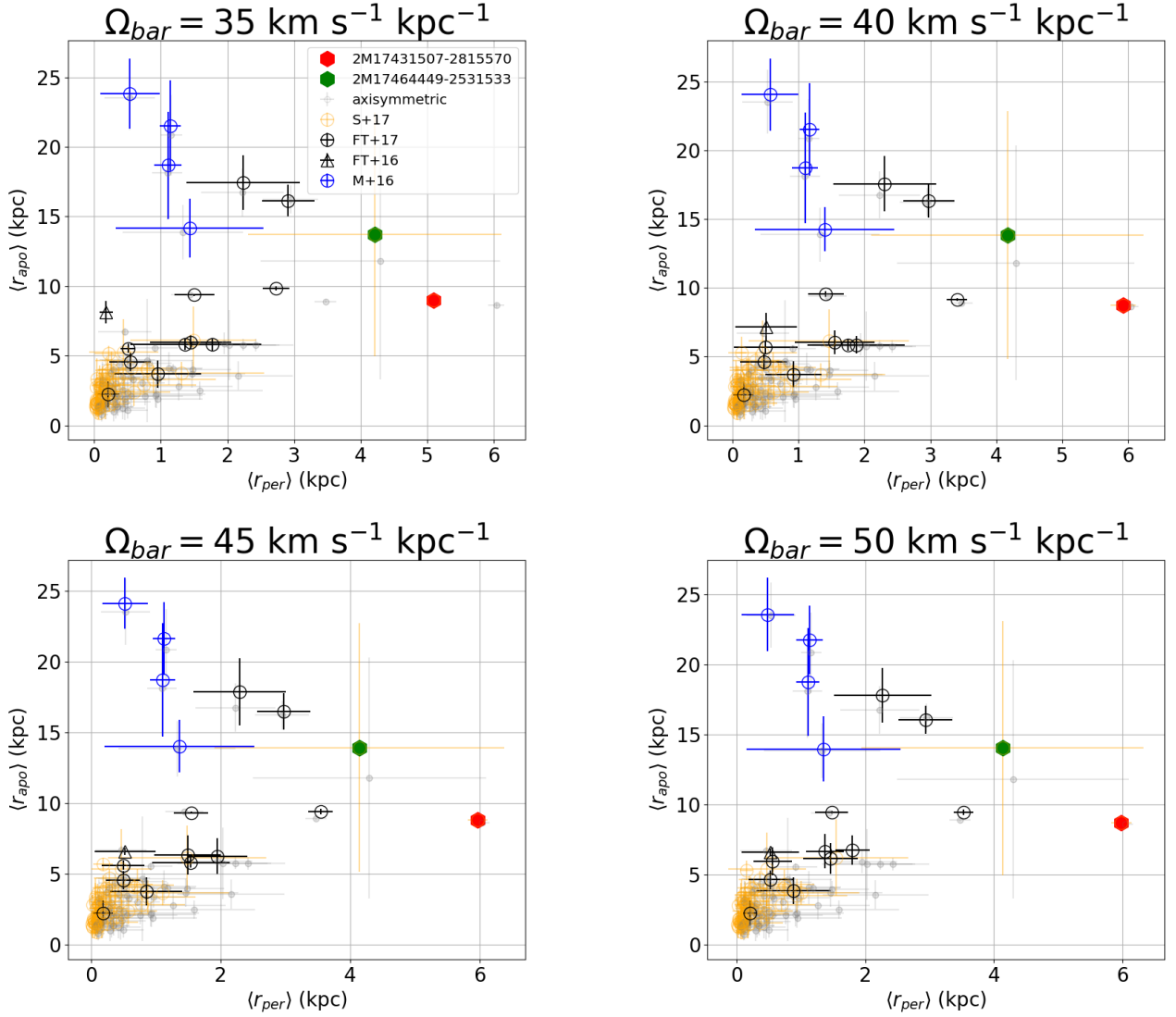


**Figure 4.** Orbital parameters as function of average perigalactic distance ( $\langle r_{per} \rangle$ ) and average apogalactic distance ( $\langle r_{apo} \rangle$ ) for the the axisymmetric model (grey dot symbols) and model with bar (with colored symbols as Figure 2).

stars (2M15113526+3551140, 2M15204588+0055032, 2M13251355-0044438 and 2M17252263+4903137) reaches large vertical excursions ( $|Z_{max}| > 25$  kpc) from the Galactic plane, and have an overall eccentricity  $\gtrsim 0.8$  (see Figures 7, 9, 8 and 10) in both an axisymmetric model and the model including the Galactic bar potential. These stars clearly resemble the halo population. Regarding the shape of their orbits, three of these stars move in a prograde sense with respect to the Galactic rotation, while one of them has an orbit with retrograde motion, we expect most of these stars having different orbital configurations from the rest, because it belongs to the halo component. With respect to the different values of the bar patterns speed, we can

see that most orbits are not sensitive to the change of this parameter, except for TYC 5619-109-1 as discussed above.

Regarding, the newly N-rich stars identified in (Fernández-Trincado et al. 2017c), we found most of them (10 out of 11 stars) in prograde sense with respect to the Galactic rotation, except one star (2M02491285+5534213) with clear signature of retrograde motion as illustrated in Figure 5. This star dynamically resembles a (inner) halo star given its high vertical excursion from the plane with  $|Z_{max}| \lesssim 7.6$  kpc, and higher eccentricity ( $e \gtrsim 0.7$ ), the orbit is clearly going inside and outside of the bulge region in a higher-order resonance (see Figure 7 and 8). Furthermore, we found four objects (2M17535944+4708092, 2M12155306+1431114,

2M16062302–1126161 and 2M11462612–1419069 ) from our subsample of N-rich stars are likely to be on higher eccentric ( $e \gtrsim 0.5$ ) in a prograde motion sense respect to the rotation of the bar and reaching out to maximum distances from the Galactic plane,  $|Z_{max}|$ , larger than 3.8 kpc and orbital excursions going inside and outside CR (see Figure 7), these orbital properties are typically found in halo stars and Galactic globular clusters. While a few of them (6 out of 11 stars) have prograde orbits with low vertical excursions from the Galactic plane ( $|Z_{max}| \lesssim 2$  kpc) and relatively higher eccentricities ( $e > 0.5$ ). More interestingly, two of those stars (2M17492967–2328298 and 2M17454705–2639109) appear to behave as bar-like orbits; two possible interpretations are that these objects are formed from a recent gas accretion event and born from a relatively pristine gas (see Chiappini et al. 2015) or else, a more plausible interpretation is to assume that they were likely kicked out of globular cluster systems trapped into the bar potential (Kunder et al. 2018; Minniti et al. 2018). On the other hand, four of these stars with prograde motion exhibit disk-like orbits moving around the Lagrange points  $L_4$  and  $L_5$ , and orbits that move around CR for a while until they get trapped by the  $L_4$  and  $L_5$  Lagrange point as illustrated in Figure 7.

Figure 6 shows the distribution of each orbital parameter (eccentricity, perigalactic distance, apogalactic distance and the maximum vertical excursion from the Galactic plane), for the axisymmetric model and the model with bar using a  $\Omega_{bar} = 35, 40, 45$  and  $50 \text{ km s}^{-1} \text{ kpc}^{-1}$ . As may be seen in this figure, most of the N-rich lies in orbital configurations that spans a wider range in high eccentricities (0.4–1) in the axisymmetric model, with a significant fraction of them have retrograde sense (see cyan histograms in the same figure) with respect to the direction of the Galactic rotation, this indicates that the majority of the N-rich stars, especially those towards the inner Galaxy are actually an inner halo-bulge sample, and have similar dynamical behaviour as compared to Galactic globular clusters. We can also notice that the Galactic bar model (*non-axisymmetric*) makes the distribution in eccentricities to be narrower than with the axisymmetric model, whereas the orbits become highly eccentric with the presence of the bar ( $> 0.5$ ), which contains a significant fraction of the N-rich population in retrograde orbits. In the case of the non-axisymmetric model, we found a different behaviour as compared with other N-rich stars, i.e., an important fraction of the stars have the correct energy to have prograde and retrograde orbits at the same time that spans a wider range in high eccentricities similar to the axisymmetric case, which could be related to a chaotic behavior associated with an early phase of evolution of the inner regions of the Milky Way (Pérez-Villegas et al. 2017), meaning that the majority of the N-rich stars were formed in a very early stage of the Milky Way, before bar formation, thus supporting the globular cluster escapee scenario (Fernández-Trincado et al. 2016a; Savino & Posti 2019; Khoperskov et al. 2018).

#### 4 CONCLUDING REMARKS

In this work we have employed accurate data from the The European Space Agency’s Gaia mission Second Data Release (DR2) and APOGEE-2 survey to present the first dynamical

characterisation of giant stars with anomalously high levels of  $[\text{N}/\text{Fe}]$  toward the bulge and halo of the Milky Way. This analysis have been carried out with the Milky Way model called **GravPot16**, where the orbits are integrated in both an full axisymmetric configuration of the model and a configuration including the Galactic bar potential, where we vary the angular velocity of the bar. The inclusion of a more realistic (as far as possible) rotating Galactic “bar/bulge” proved to be essential on the description of the dynamical behavior of N-rich stars across of the Milky Way, particularly in the N-rich sample located in the inner Galaxy, which shows a low eccentricity with no bar, whereas the orbits become highly eccentric with the presence of the bar, which in turn depends on the angular velocity, i.e., higher if  $\Omega_{bar} < 40 \text{ km s}^{-1}$  or lower if  $\Omega_{bar} > 40 \text{ km s}^{-1}$ . From Figure 6, we can see that the Galactic bar induces to have smaller average perigalactic and apogalactic distances, and higher eccentricities. By this, it is very likely that either these peculiar population was formed early on before bar formation, or else was formed together with the bar. The main results can be summarized as follows:

- Our models predict that a significant fraction ( $\sim 54\%$ ) of the N-rich stars have orbits with retrograde sense with respect to the direction of the Galactic rotation in the axisymmetric model, while than  $>41\%$  have a particular and different behaviour, whose orbits change their sense of motion from retrograde to prograde with respect to the rotation of the bar, depending on the bar angular velocity,  $\Omega_{bar}$ . This dynamical behaviour confirm that most of the N-rich giant belonged to a distinct population of the Milky Way, likely associated with accreted material and formed in a very early stage of the Galaxy, before bar formation. This provides observational support for the idea that most of the N-rich stars, especially those towards the inner Galaxy, may have been assembled by kicking out globular cluster stars, causing it to be now observed as a part of the inner Galactic halo.
- We can also notice that a minority,  $\sim 10\%$  of the N-rich stars within the bulge area, were identified in orbits that follow the bar structure, and share the orbital properties of the “bar/bulge”, whose orbits are trapped by different resonances, depending on the bar angular velocity,  $\Omega_{bar}$ , similar to some bulge globular clusters such as M 62 (see Minniti et al. 2018). It is likely, that these N-rich stars were formed before bar formation, and were trapped during or together the bar formation, as envisioned by (Pérez-Villegas et al. 2018).
- We found that approximately 46% of our sample follows high eccentric ( $e \gtrsim 0.6$ ) prograde orbits with the presence of the bar, which depends on the bar pattern speeds, higher considering a slow-rotating bar ( $\Omega_{bar} \sim 35 \text{ km s}^{-1} \text{ kpc}^{-1}$ ) or lower for a fast-rotating bar ( $\Omega_{bar} \sim 50 \text{ km s}^{-1} \text{ kpc}^{-1}$ ). On the other hand, the non-axisymmetric model (with a bar/bulge model) makes the distribution in eccentricities to be narrower than with the full axisymmetric configuration of our model. On the other hands, for most of the N-rich stars inside the CR, the orbits have a particular and different behaviour, e.g., the orbits are trapped by a higher-order resonance or corotation, depending on the bar pattern speed,  $\Omega_{bar}$ , this means that most orbits are sensitive to the change of this parameter, which is negligible for stars whose orbits reach distance beyond the Sun’s Galactocentric

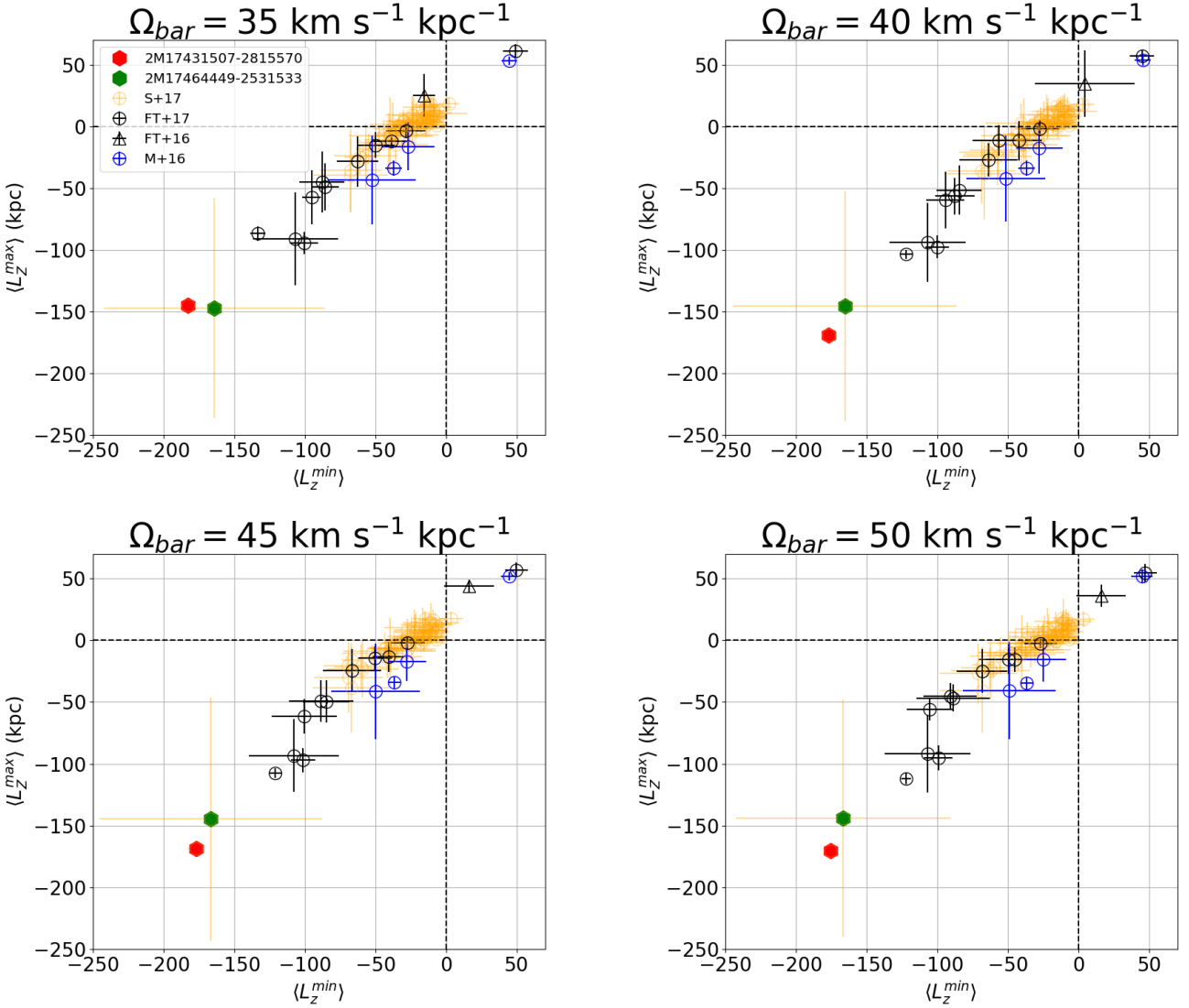


**Figure 5.** Average of the maximum and minimal z-component  $L_z$  in the inertial frame in the model with nonaxisymmetric structures.

distance. This prove that of the bar/bulge is essential for the description of the dynamical behavior of these N-rich stars in the inner Galaxy.

- We also identified two N-rich stars, 2M174644492531533 and 2M174315072815570, with larger apogalocentric distances  $\gtrsim 9$  kpc and lower vertical excursion from the Galactic plane ( $\lesssim 2$ ) kpc, and appear to behave as halo-like orbits, the most likely is that these two stars are inner halo interlopers that happens to be at same distance and location as where bulge N-rich stars reside, and this means that halo contamination could be not insignificant when studying chemically anomalous stars found within the bulge region (e.g., see [Recio-Blanco et al. 2017](#)).

## REFERENCES

- Abolfathi B., et al., 2018, *ApJS*, **235**, 42  
 Albareti F. D., et al., 2017, *ApJS*, **233**, 25  
 Altmann M., Catelan M., Zoccali M., 2005, *A&A*, **439**, L5  
 Arenou F., et al., 2018, *A&A*, **616**, A17  
 Blanton M. R., et al., 2017, *AJ*, **154**, 28  
 Brunthaler A., et al., 2011, *Astronomische Nachrichten*, **332**, 461  
 Carollo D., et al., 2010, *ApJ*, **712**, 692  
 Carollo D., Martell S. L., Beers T. C., Freeman K. C., 2013, *ApJ*, **769**, 87  
 Chiappini C., et al., 2015, *A&A*, **576**, L12  
 Einasto J., 1979, in Burton W. B., ed., *IAU Symposium Vol. 84, The Large-Scale Characteristics of the Galaxy*. pp 451–458  
 Fehlbeg E., 1968, *NASA Technical Report*, p. 315  
 Fernández-Trincado J. G., Vivas A. K., Mateu C. E., Zinn R., Robin A. C., Valenzuela O., Moreno E., Pichardo B., 2015a,

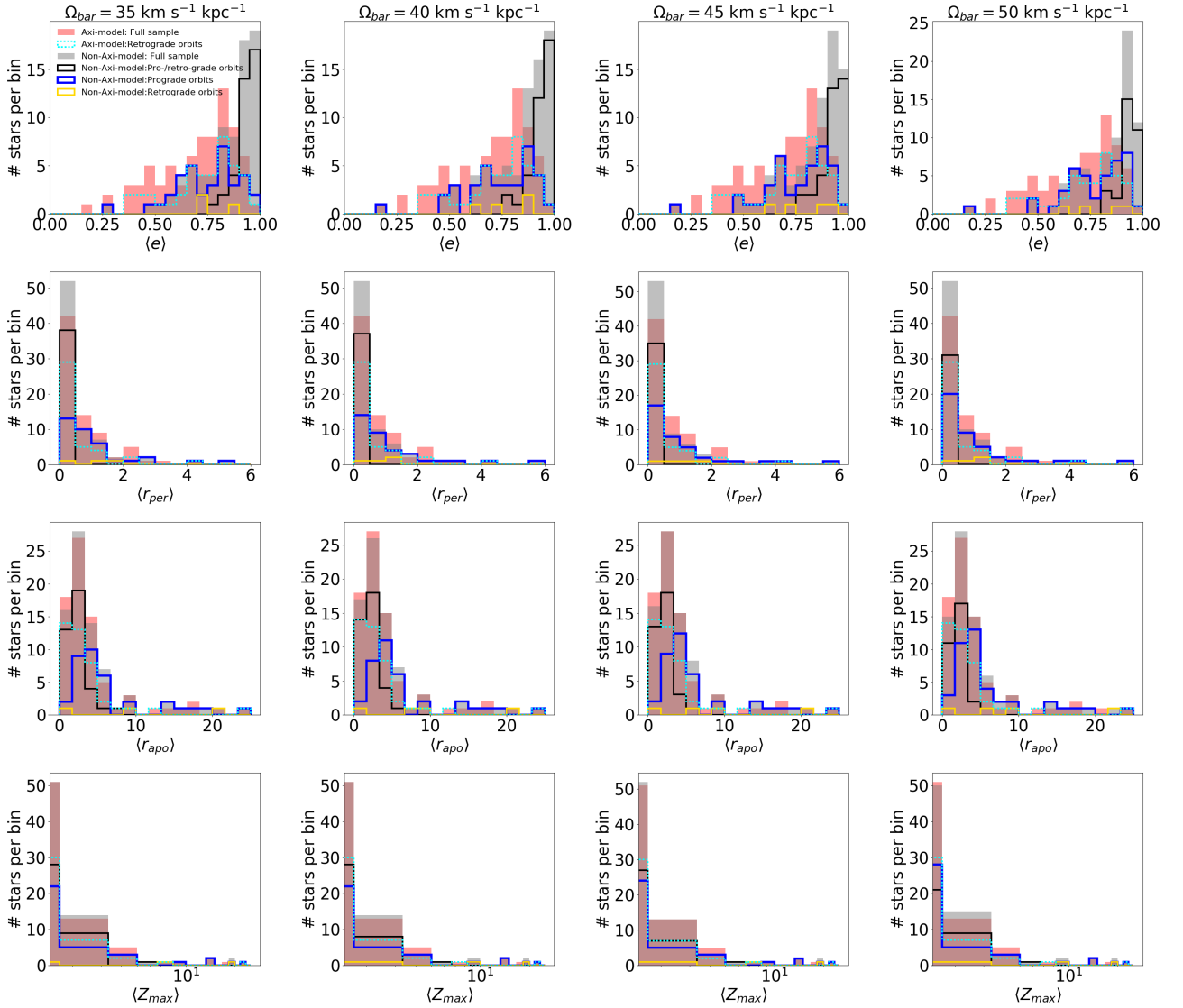


**Figure 6.** Histograms of the corresponding average orbital parameters, showing the estimated dynamical properties of our sample. Orbital elements computed in the *axisymmetric configuration* of *GravPot16* are shown, where the red and cyan histograms correspond to the full sample and the fraction of stars in retrograde sense with respect to the direction of the Galactic rotation, respectively. Orbital solutions from the *non-axisymmetric configuration* are also shown, where the grey, black, blue and gold correspond to the full sample, the fraction of stars that have prograde and retrograde orbits at the same time, the fraction of stars in prograde sense with respect to the rotation of the bar and the fraction of stars in retrograde sense of motion, respectively.

*A&A*, 574, A15

Fernández-Trincado J. G., et al., 2015b, *A&A*, 583, A76

Fernández-Trincado J. G., Robin A. C., Reylé C., Vieira K., Palmer M., Moreno E., Valenzuela O., Pichardo B., 2016a, *MNRAS*, 461, 1404

Fernández-Trincado J. G., et al., 2016b, *ApJ*, 833, 132

Fernández-Trincado J. G., Robin A. C., Moreno E., Pérez-Villegas A., Pichardo B., 2017a, in Reylé C., Di Matteo P., Herpin F., Lagadec E., Lançon A., Meliani Z., Royer F., eds, SF2A-2017: Proceedings of the Annual meeting of the French Society of Astronomy and Astrophysics. pp 193–198 ([arXiv:1708.05742](https://arxiv.org/abs/1708.05742))

Fernández-Trincado J. G., Geisler D., Moreno E., Zamora O., Robin A. C., Villanova S., 2017b, in Reylé C., Di Matteo P., Herpin F., Lagadec E., Lançon A., Meliani Z., Royer F., eds, SF2A-2017: Proceedings of the Annual meeting of the French Society of Astronomy and Astrophysics. pp 199–202 ([arXiv:1710.07433](https://arxiv.org/abs/1710.07433))

Fernández-Trincado J. G., et al., 2017c, *ApJ*, **846**, L2

Fernández-Trincado J. G., et al., 2019, arXiv e-prints,

Gaia Collaboration et al., 2018, *A&A*, **616**, A1

García Pérez A. E., et al., 2016, *AJ*, **151**, 144

Gilmore G., et al., 2012, *The Messenger*, **147**, 25

Gunn J. E., et al., 2006, *AJ*, **131**, 2332

Helmi A., Babusiaux C., Koppelman H. H., Massari D., Veljanoski J., Brown A. G. A., 2018, *Nature*, **563**, 85

Holtzman J. A., et al., 2015, *AJ*, **150**, 148

Holtzman J. A., et al., 2018, *AJ*, **156**, 125

Ibata R. A., Malhan K., Martin N. F., 2019, *ApJ*, **872**, 152

Jönsson H., et al., 2018, *AJ*, **156**, 126

Khoperskov S., Mastrobuono-Battisti A., Di Matteo P., Haywood M., 2018, *A&A*, **620**, A154

Koch A., Grebel E. K., Martell S. L., 2019, arXiv e-prints,

Koppelman H., Helmi A., Veljanoski J., 2018, *ApJ*, **860**, L11

Kunder A., et al., 2014, *A&A*, **572**, A30

Kunder A., et al., 2018, *AJ*, **155**, 171

Leung H. W., Bovy J., 2019, arXiv e-prints,

Libralato M., et al., 2018, *ApJ*, **854**, 45

Lind K., et al., 2015, *A&A*, **575**, L12

Lindgren L., et al., 2018, *A&A*, **616**, A2

Majewski S. R., et al., 2017, *AJ*, **154**, 94

Martell S. L., Grebel E. K., 2010, *A&A*, **519**, A14

Martell S. L., Smolinski J. P., Beers T. C., Grebel E. K., 2011, *A&A*, **534**, A136

Martell S. L., et al., 2016, *ApJ*, **825**, 146

Minniti D., Fernández-Trincado J. G., Ripepi V., Alonso-García J., Contreras Ramos R., Marconi M., 2018, *ApJ*, **869**, L10

Moreno E., Pichardo B., Schuster W. J., 2015, *MNRAS*, **451**, 705

Nidever D. L., et al., 2015, *AJ*, **150**, 173

Nissen P. E., Schuster W. J., 2010, *A&A*, **511**, L10

Pancino E., et al., 2017, *A&A*, **601**, A112

Pereira C. B., Smith V. V., Drake N. A., Roig F., Hasselquist S., Cunha K., Jilinski E., 2017, *MNRAS*, **469**, 774

Pérez-Villegas A., Portail M., Gerhard O., 2017, *MNRAS*, **464**, L80

Pérez-Villegas A., Rossi L., Ortolani S., Casotto S., Barbuy B., Bica E., 2018, *Publ. Astron. Soc. Australia*, **35**, e021

Pichardo B., Martos M., Moreno E., 2004, *ApJ*, **609**, 144

Queiroz A. B. A., et al., 2018, *MNRAS*, **476**, 2556

Randich S., Gilmore G., Gaia-ESO Consortium 2013, *The Messenger*, **154**, 47

Recio-Blanco A., et al., 2017, *A&A*, **602**, L14

Reis I., Poznanski D., Baron D., Zasowski G., Shahaf S., 2018, *MNRAS*, **476**, 2117

Robin A. C., Reylé C., Derrière S., Picaud S., 2003, *A&A*, **409**, 523

Robin A. C., Marshall D. J., Schultheis M., Reylé C., 2012, *A&A*, **538**, A106

Robin A. C., Reylé C., Fliri J., Czekaj M., Robert C. P., Martins A. M. M., 2014, *A&A*, **569**, A13

Savino A., Posti L., 2019, arXiv e-prints,

Schiappacasse-Ulloa J., et al., 2018, *AJ*, **156**, 94

Schiavon R. P., et al., 2017, *MNRAS*, **465**, 501

Tang B., et al., 2018, *ApJ*, **855**, 38

Tang B., Liu C., Fernández-Trincado J. G., Geisler D., Shi J., Zamora O., Worthey G., Moreno E., 2019, *ApJ*, **871**, 58

Taylor M. B., 2005, in Shopbell P., Britton M., Ebert R., eds, *Astronomical Society of the Pacific Conference Series Vol. 347, Astronomical Data Analysis Software and Systems XIV*. p. 29

Vasiliev E., 2018, arXiv e-prints,

Zamora O., et al., 2015, *AJ*, **149**, 181

Zasowski G., et al., 2013, *AJ*, **146**, 81

Zasowski G., et al., 2017, *AJ*, **154**, 198

## ACKNOWLEDGMENTS

We would like to thank the referee for insightful comments that helped to improve this work. This article is based upon work from the ChETEC COST Action (CA16117), supported by COST (European Cooperation in Science and Technology). J.G.F-T is supported by FONDECYT No. 3180210. J.G.F-T acknowledges the use of TOPCAT (Taylor 2005) through out the course of this investigation. APV acknowledges a FAPESP for the postdoctoral fellowship grant no. 2017/15893-1 and the DGAPA-PAPIIT grant IG100319.

Funding for the **GravPot16** software has been provided by the Centre national d'études spatiales (CNES) through grant 0101973 and UTINAM Institute of the Université de Franche-Comté, supported by the Région de Franche-Comté and Institut des Sciences de l'Univers (INSU). Simulations have been executed on computers from the Utinam Institute of the Université de Franche-Comté, supported by the Région de Franche-Comté and Institut des Sciences de l'Univers (INSU), and on the supercomputer facilities of the Mésocentre de calcul de Franche-Comté.

This work presents results from the European Space Agency (ESA) space mission Gaia. Gaia data are being processed by the Gaia Data Processing and Analysis Consortium (DPAC). Funding for the DPAC is provided by national institutions, in particular the institutions participating in the Gaia MultiLateral Agreement (MLA). The Gaia mission website is <https://www.cosmos.esa.int/gaia>. The Gaia archive website is <https://archives.esac.esa.int/gaia>.

Funding for the Sloan Digital Sky Survey IV has been provided by the Alfred P. Sloan Foundation, the U.S. Department of Energy Office of Science, and the Participating Institutions. SDSS-IV acknowledges support and resources from the Center for High-Performance Computing at the University of Utah. The SDSS web site is [www.sdss.org](http://www.sdss.org). SDSS-IV is managed by the Astrophysical Research Consortium for the Participating Institutions of the SDSS Collaboration including the Brazilian Participation Group, the Carnegie Institution for Science, Carnegie Mellon University, the Chilean Participation Group, the French Participation Group, Harvard-Smithsonian Center for Astrophysics, Instituto de Astrofísica de Canarias, The Johns Hopkins University, Kavli Institute for the Physics and Mathematics of the Universe (IPMU) / University of Tokyo, Lawrence Berkeley National Laboratory, Leibniz Institut für Astrophysik Potsdam (AIP), Max-Planck-Institut für Astronomie (MPIA Heidelberg), Max-Planck-Institut für Astrophysik (MPA Garching), Max-Planck-Institut für Extraterrestrische Physik (MPE), National Astronomical Observatory of China, New Mexico State University, New York University, University of Dame, Observatório Nacional / MCTI, The Ohio State University, Pennsylvania State University, Shanghai Astronomical Observatory, United Kingdom Participation Group, Universidad Nacional Autónoma de México, University of Arizona, University of Colorado Boulder, University of Oxford, University of Portsmouth, University of Utah, University of Virginia, University of Washington, University of Wisconsin, Vanderbilt University, and Yale University.

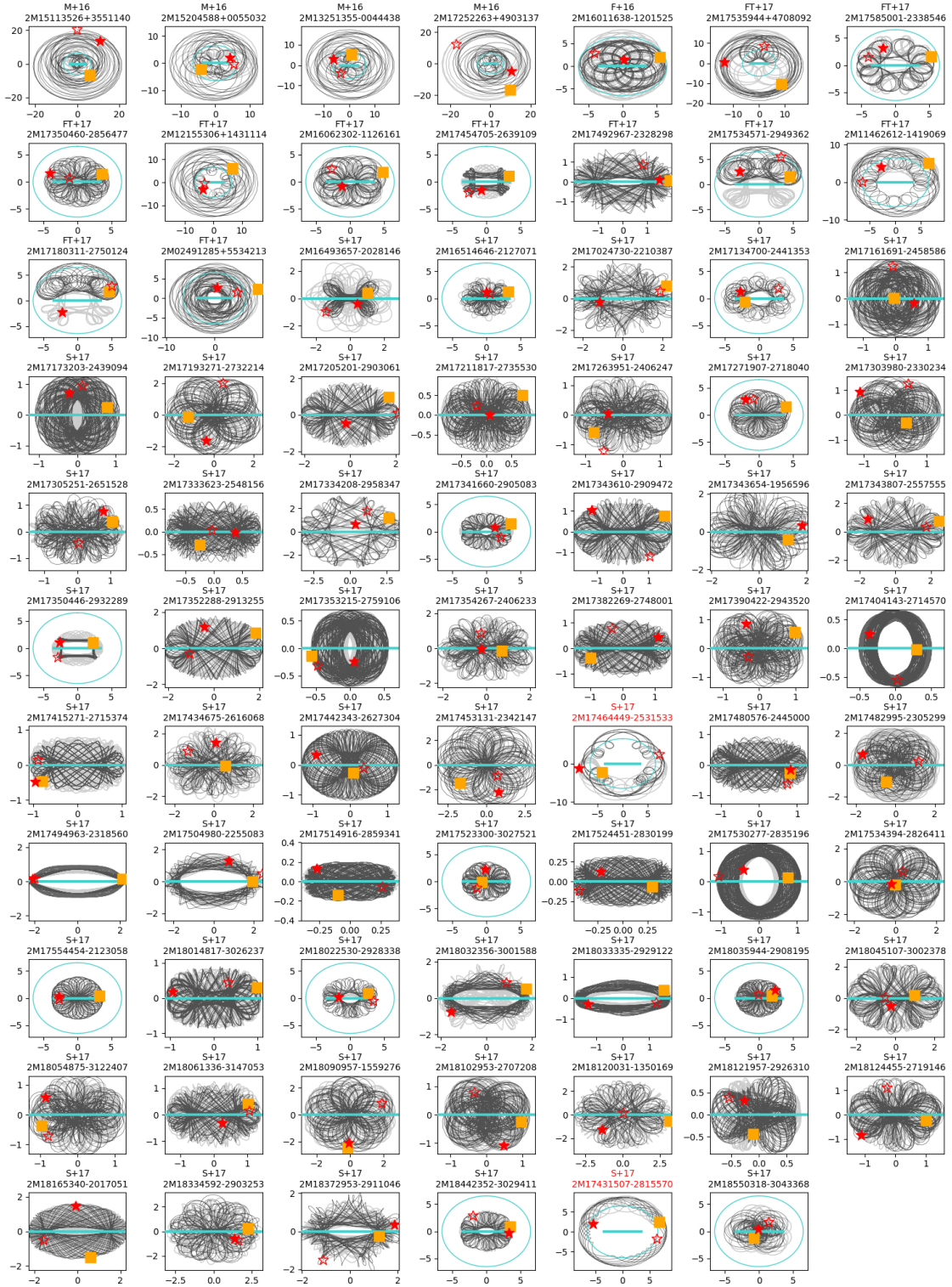


**Figure 7.** Orbital solutions in the non-axisymmetric model: Orbits for the sample of N-rich stars in X–Y projection in the potential with a slowly bar (grey line),  $\Omega_{\text{bar}} = 35 \text{ km s}^{-1} \text{ kpc}^{-1}$  and a faster bar (black line),  $\Omega_{\text{bar}} = 50 \text{ km s}^{-1} \text{ kpc}^{-1}$ . The cyan solid line shows the size of the Galactic bar, and the cyan big circle the co-rotation radius,  $\text{CR} \sim 6.5 \text{ kpc}$ . The small square symbol marks the present position of the star, and the red open and filled square marks its final position in the potential with slow and faster bar, respectively. The title indicate the origin of the star, M+16: Martell et al. (2016), FT+16: Fernández-Trincado et al. (2016b), S+17: Schiavon et al. (2017) and FT+17: Fernández-Trincado et al. (2017c), while the subtitle indicate the APOGEE id of each star. The title highlighted in red mark the stars: 2M17431507–2815570 and 2M17464449–2531533 (see text).

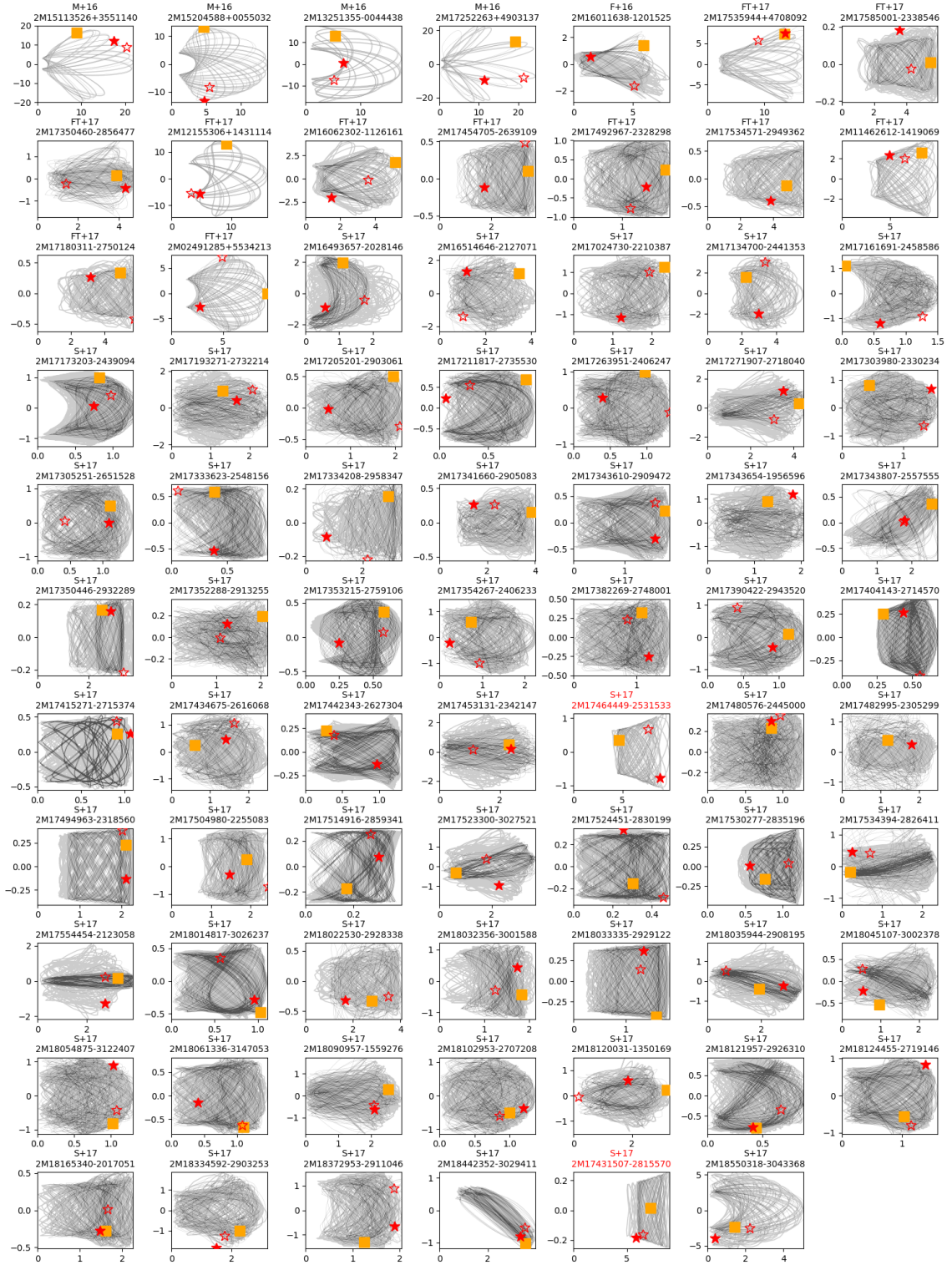
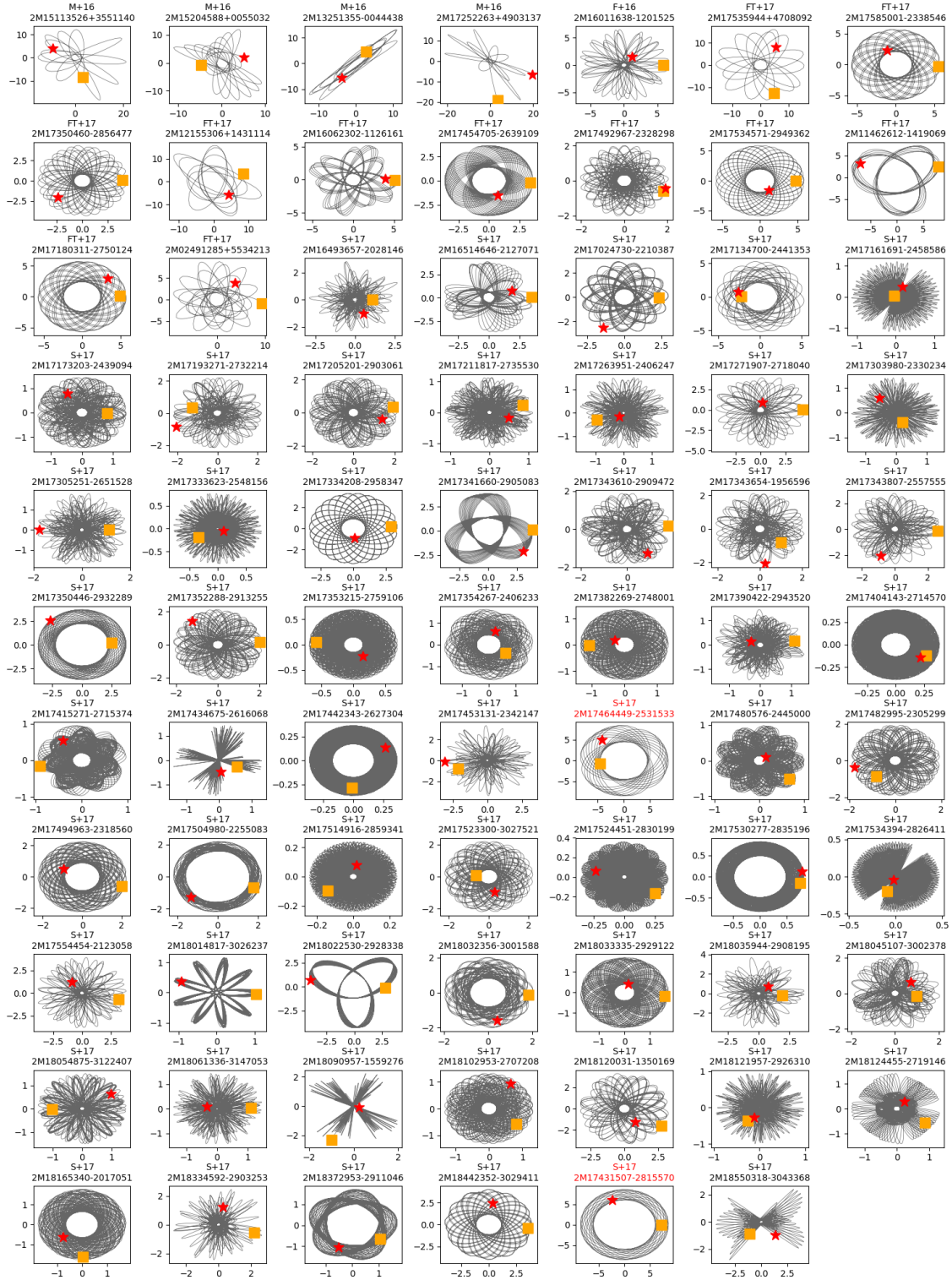


Figure 8. Orbital solutions in the non-axisymmetric model: R-z projection for the same sample as arranged in Figure 7.



**Figure 9.** Orbital solutions in the axisymmetric model: X–Y projection for the same sample as arranged in Figure 7.

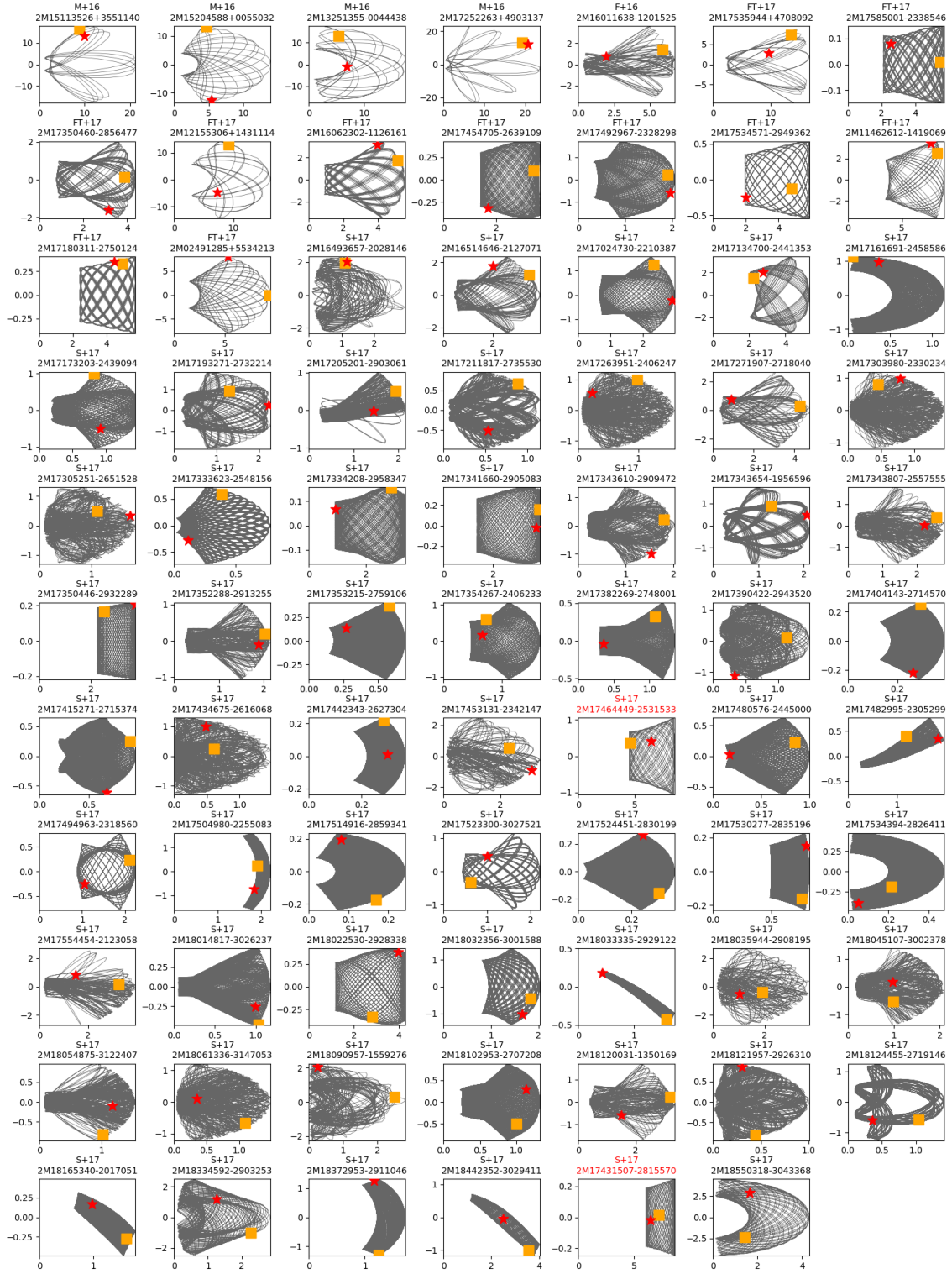


Figure 10. Orbital solutions in the axisymmetric model: R-z projection for the same sample as arranged in Figure 7.